

# Observations of Clouds, Aerosols, Precipitation, and Surface Radiation over the Southern Ocean

## An Overview of CAPRICORN, MARCUS, MICRE, and SOCRATES

Greg M. McFarquhar, Chris Bretherton, Roger Marchand, Alain Protat, Paul J. DeMott, Simon P. Alexander, Greg C. Roberts, Cynthia H. Twohy, Darin Toohey, Steve Siems, Yi Huang, Robert Wood, Robert M. Rauber, Sonia Lasher-Trapp, Jorgen Jensen, Jeff Stith, Jay Mace, Junshik Um, Emma Järvinen, Martin Schnaiter, Andrew Gettelman, Kevin J. Sanchez, Christina S. McCluskey, Lynn M. Russell, Isabel L. McCoy, Rachel Atlas, Charles G. Bardeen, Kathryn A. Moore, Thomas C. J. Hill, Ruhi S. Humphries, Melita D. Keywood, Zoran Ristovski, Luke Cravigan, Robyn Schofield, Chris Fairall, Marc D. Mallet, Sonia M. Kreidenweis, Bryan Rainwater, John D'Alessandro, Yang Wang, Wei Wu, Georges Saliba, Ezra J. T. Levin, Saisai Ding, Francisco Lang, Son C. H. Truong, Cory Wolff, Julie Haggerty, Mike J. Harvey, Andrew Klekociuk, and Adrian McDonald

<https://doi.org/10.1175/BAMS-D-20-0132.2>

Corresponding author: Greg M. McFarquhar, mcfarq@ou.edu

This document is a supplement to <https://doi.org/10.1175/BAMS-D-20-0132.1>

©2021 American Meteorological Society

For information regarding reuse of this content and general copyright information, consult the [AMS Copyright Policy](#).

**AFFILIATIONS:** **McFarquhar and D'Alessandro**—Cooperative Institute for Mesoscale Meteorological Studies, and School of Meteorology, University of Oklahoma, Norman, Oklahoma; **Bretherton, Marchand, Wood, McCoy, and Atlas**—Department of Atmospheric Sciences, University of Washington, Seattle, Washington; **Protat**—Australian Bureau of Meteorology, Melbourne, Victoria, and Australian Antarctic Programme Partnership, Institute for Marine and Antarctic Science, University of Tasmania, Hobart, Tasmania, Australia; **DeMott, Moore, Hill, and Kreidenweis**—Department of Atmospheric Science, Colorado State University, Fort Collins, Colorado; **Alexander and Klekociuk**—Australian Antarctic Division, and Australian Antarctic Programme Partnership, Institute for Marine and Antarctic Science, University of Tasmania, Hobart, Tasmania, Australia; **Roberts**—Scripps Institution of Oceanography, La Jolla, California, and Centre National de Recherches Météorologiques, UMR3589, Toulouse, France; **Twohy**—NorthWest Research Associates, Redmond, Washington, and Scripps Institution of Oceanography, La Jolla, California; **Toohey and Rainwater**—Department of Atmospheric and Oceanic Sciences, University of Colorado Boulder, Boulder, Colorado; **Siems, Lang, and Truong**—School of Earth, Atmosphere and Environment, Monash University, Melbourne, Victoria, Australia; **Huang and Schofield**—School of Earth Sciences, University of Melbourne, Melbourne, Victoria, Australia; **Rauber and Lasher-Trapp**—Department of Atmospheric Sciences, University of Illinois at Urbana–Champaign, Urbana, Illinois; **Jensen, Stith, Gettelman, McCluskey, Bardeen, Wolff, and Haggerty**—National Center for Atmospheric Research, Boulder, Colorado; **Mace**—University of Utah, Salt Lake City, Utah; **Um**—Cooperative Institute for Mesoscale Meteorological Studies, University of Oklahoma, Norman, Oklahoma, and Department of Atmospheric Sciences, Pusan National University, Pusan, South Korea; **Järvinen**—National Center for Atmospheric Research, Boulder, Colorado, and Karlsruhe Institute of Technology, Karlsruhe, Germany; **Schnaiter**—Karlsruhe Institute of Technology, Karlsruhe, Germany; **Sanchez, Russell, and Saliba**—Scripps Institution of Oceanography, La Jolla, California; **Humphries and Keywood**—Climate Science Centre, Oceans and Atmosphere, CSIRO, Melbourne, Victoria, Australia; **Ristovski and Cravigan**—School of Earth and Atmospheric Sciences, Queensland University of Technology, Brisbane, Queensland, Australia; **Fairall**—NOAA, Boulder, Colorado; **Mallet**—Australian Antarctic Programme Partnership, Institute for Marine and Antarctic Science, University of Tasmania, Hobart, Tasmania, Australia; **Wang**—Cooperative Institute for Mesoscale Meteorological Studies, University of Oklahoma, Norman, Oklahoma, and Beijing Normal University, Beijing, China; **Wu**—Cooperative Institute for Mesoscale Meteorological Studies, University of Oklahoma, Norman, Oklahoma; **Levin**—Department of Atmospheric Science, Colorado State University, Fort Collins, and Handix Scientific, Boulder, Colorado; **Saisai Ding**—Peking University, Beijing, China; **Harvey**—National Institute of Water and Atmospheric Research, Wellington, New Zealand; **McDonald**—Gateway Antarctica, and School of Physical and Chemical Sciences, University of Canterbury, Christchurch, New Zealand

In this supplement, more detailed information is given about the instrument suites used during the different campaigns, the performance of the different instruments, the meteorological conditions sampled, the modeling studies conducted, and extra details about some observations.

### Instrumentation, data acquisition, and derived products

Table ES1 lists the instrumentation used during MICRE. Much of the MICRE instrumentation was operational by 2 April 2016. But, many instruments suffered some difficulties or down time, and in several cases instruments had to be replaced during the next spring or fall resupply voyage of the AA. Table ES2 lists time periods for which high-quality observations are available for each instrument. Further, note that the W-band radar, the Bistatic Radar System for Atmospheric Studies (BASTA; Delanoë et al. 2016), is the same radar installed on R/V *Investigator* during CAPRICORN I and II (Mace and Protat 2018a). The radar was deployed for the first year of MICRE, and afterward relocated to the R/V *Investigator* for CAPRICORN II. There were three overflights of the NCAR G-V over Macquarie Island on 31 January, 4 February, and 19 February 2018, giving data for comparison between MICRE and SOCRATES.

Table ES1. List of instruments used during MICRE.

Instrument name/operating organization	Instrument description	Primary measurement	Derived quantities
DOE Sky Radiation Radiometers (SKYRAD)	Radiometers providing continuous measurements of downwelling irradiances	Broadband SW and LW downwelling irradiance	Cloud fraction
DOE Ground Radiation Radiometers (GNDRAD)	Radiometers on stand providing continuous measurements of upwelling irradiances	Broadband SW reflected and LW upwelling irradiance	Surface skin temperature
DOE ceilometer	Remote sensor transmitting and receiving near-infrared pulses of radiation	Light scattered by clouds, precipitation and aerosols	Cloud-base height, boundary layer height
DOE Microwave Radiometer (MWR)	Sensitive microwave receiver that measures radiance at 23.8 and 31.4 GHz	Brightness temperature at two frequencies	Column integrated liquid water and water vapor
DOE Parsivel disdrometer	Laser optical device for measuring raindrop size and fall speed	Fall speed and size of raindrops	Raindrop size distribution, precipitation rate, radar reflectivity
DOE CIMEL sun photometer	Multichannel automatic sun- and sky-scanning radiometer	Direct solar irradiance and sky radiance at Earth's surface	Aerosol optical depth or cloud optical depth
BASTA BoM W-band Cloud Radar	Vertically pointing 95-GHz cloud radar	Vertical profiles (1 min, 25 m) of calibrated 95-GHz radar reflectivity and Doppler velocity	Cloud mask, cloud fraction, thermodynamic phase (with lidar)
AAD polarization lidar	Active ground-based sensor transmitting and receiving pulses of radiation at 532 nm[1]	Backscatter return and polarization	Height of aerosol and cloud layers and derived quantities (optical depth, phase, particle size, etc.)
Canterbury ceilometer	Remote sensing instrument transmitting and receiving infrared light pulses	Receiver detects amount of light scattered by clouds and precipitation	Cloud height, vertical visibility, and planetary boundary layer height
CSU aerosol filter samples	Filters for ice nucleating particle measurements and next generation bacterial sequencing studies	Ice nucleating particle number concentration freezing temperature spectra; genetic sequences of aerosol bacteria	Analyzed ice nucleating particle number concentrations and bacterial biodiversity characterizations over 21–62 h

The instruments used in CAPRICORN I are listed in Table ES3, and most instruments operated near 100% of the time. Aerosol volatility was measured using a volatility tandem differential mobility analyzer (V-TDMA; Johnson et al. 2004) operated at 250°C and can be used to infer aerosol composition. In pristine marine environments volatility is useful for distinguishing between the semivolatile secondary/non-sea salt sulfates and the low volatility primary sea spray. A hygroscopicity tandem differential mobility analyzer (H-TDMA; Johnson et al. 2008) was used to measure the subsaturated aerosol hygroscopicity (at 90% relative humidity), an important variable for aerosol activation to CCN. The influence of ship emissions and continental transport have been removed from these data by applying an hourly average black carbon threshold 30 ng m<sup>-3</sup>, a radon threshold of 150 kBq m<sup>-3</sup>, a particle number threshold of 5,000 cm<sup>-3</sup>, and limiting the measurements to periods when the wind was in the sector from 240° to 120° relative to the ship direction. Of particular interest for the SO projects is processes occurring in the cold dry sector of cyclones. Using surface pressure fields from ERA5 and calculating the position of cold fronts following Simmonds et al. (2012), there were five incidences when R/V *Investigator* was in the cold sector of major cold fronts. Dates and approximate duration are shown in Table ES4.

As described in Mace and Protat (2018a), the first voyage can be divided into two periods, the first occurring from 15 to 27 March 2016 when the ship serviced oceanic buoys near 47°S and 142°E, and the second after 28 March 2016 when the ship spent time sampling a cold (30 March–5 April) and a warm (6–10 April) mesoscale oceanic eddy along the Subantarctic

**Table ES2. MICRE instruments and time periods for which high-quality observations are available, though all instruments have occasional “dropouts” where data are missing or of poor quality for a few hours or days. “PC” denotes the primary contact for non-ARM instruments; “ARM” denotes the name of the ARM datastream (which can be used to quickly find these data in the ARM data archive).**

MICRE instrumentation	Data availability	Primary references and notes
94-GHz Cloud Radar (BASTA)	2 Apr 2016–17 Mar 2017 (First year only)	Delanoë et al. (2016) Mace and Protat (2018) PC: Alain Protat (BoM)
AAD polarization lidar	7 Apr–27 Nov 2016 1 Apr 2017–4 Mar 2018	Huang et al. (2015) <b>Klekociuk et al. (2020x)</b> See footnote <sup>a</sup> PC: Simon Alexander (AAD)
Vaisala ceilometer ARM  U. Canterbury	2 Apr–14 Dec 2016 22 Feb 2017–13 Mar 2018  2 Apr 2016–13 Mar 2018	Vaisala Model CT25K Münkel et al. (2007) ARM: mcqceilS1.b1 Vaisala model CL51 Kuma et al. (2020) PC: Adrian McDonald (UC)
Microwave radiometers ARM 3 channel ARM 2 channel	2 Apr–13 Jun 2016 28 Dec 2016–13 Mar 2018	Cadeddu et al. (2013) See footnote <sup>b</sup>
ARM disdrometer OTT Parsivel <sup>2</sup>	2 Apr 2016–13 Mar 2018 See footnote <sup>c</sup>	Angulo-Martinez et al. (2018) ARM: mcqpars2S1.b1
Broadband SW and LW fluxes (SKYRAD, GNDRAD)  AAD downwelling SW and LW fluxes CIMEL sun photometer  Multifilter Rotating Shadowband Radiometer (MFRSR)	3 Apr 2016–13 Mar 2018  3 Apr 2016–9 Jan 2018 3 Apr 2016–11 Mar 2018  Failed <sup>f</sup> 21 Mar–10 Aug 2016, 15 Sep 2016–13 Mar 2018	Andreas et al. (2018) ARM: mcqskyrad60sS1.b1, mcqgnrad60sS1.b1, See footnotes <sup>d,e</sup> <b>Klekociuk et al. (2020x)</b> Holben et al. (1998) ARM: mcqcsphot ARM: mcqmfrsrS1
Other data Surface aerosol/INP filter samples  Surface CPC and CCN AAD all-sky imager  BoM radiosondes AAD surface met	Second year only  Both years Both years  Both years Both years	Nominally two samples per week DeMott et al. (2018) PC: Ruhi Humphries PC: Simon Alexander (AAD) 1-min images <b>Klekociuk et al. (2020x)</b> Twice per day, 0000 and 1200 UTC PC: Simon Alexander (AAD)

<sup>a</sup> The AAD-lidar was offline from late 2016 to early 2017 due to laser issues. Development of refined analysis products is ongoing.

<sup>b</sup> LWP and PWV retrieved via physical-iterative technique (Marchand et al. 2003) is included in the CPP-VAP product (PC: Roger Marchand). Raw brightness temperatures are in the ARM archive but be aware that there is some unusual interference noise with these data. For 3-channel MWR only instrument-level files (not netCDF) are available at present. Current plans are for the ARM standard MWRRRET retrieval to be run on the 2-channel data.

<sup>c</sup> For unknown reasons, the Parsivel reset to a previous output mode starting on 31 Oct 2016 that was incompatible with the ARM dataloggers. This resulted in bad/corrupt data in several fields. Most notably this included the precipitation rate, liquid water content, total number of particles, and weather codes. In general the Parsivel vendor's algorithm did not work well during MICRE and additional processing is underway (PC: Roger Marchand).

<sup>d</sup> Upwelling and downwelling LW fluxes are biased or bad from the start of experiment until 15 Aug 2006. Upwelling LW is suspect for several more weeks until 8 Sep 2016, but downwelling is fine after 15 Aug 2006.

<sup>e</sup> Two radiometers for broadband LW were deployed. The measurements by the two radiometers agree well except in two time windows, where radiometer 2 has a value that is 2% lower than radiometer 1 and appears to be incorrect.

<sup>f</sup> MFRSR collected data for much of the experiment, but the rotating shadow band was not initially aligned well and the rotating band eventually failed completely. Narrowband radiances during cloudy period might be used but the data are uncalibrated because of the inability to carry out a Langley analysis.

Table ES3. List of instruments used in CAPRICORN I.

Instrument name/operating organization	Instrument description	Primary measurement	Derived quantities
<b>Clouds and precipitation</b>			
BoM W-band Cloud Radar (BASTA)	Vertically pointing 95-GHz cloud radar	Vertical profiles (12 s, 25 m) of calibrated 95-GHz radar reflectivity and Doppler velocity	Cloud mask, cloud fraction, thermodynamic phase (with lidar)
BoM lidar (RMAN-511)	Vertically pointing 355-nm cloud and aerosol backscatter lidar	Vertical profiles (2 min, 15 m) of calibrated lidar co-polar and cross-polar backscatter, depolarization ratio	Cloud mask, cloud fraction, thermodynamic phase (with cloud radar)
University of Utah 2-channel microwave radiometer (MWR)	2-channel microwave radiometer	20.6- and 31.2-GHz brightness temperatures	Liquid water path, water vapor path
Duke University Micro Rain Radar (MRR-2)	Vertically pointing 24-GHz rain radar	Vertical profiles (10 s, 50 m) of 24-GHz radar reflectivity, Doppler velocity, and spectral width	Vertical profiles of precipitation rate, DSD parameters
University of Hamburg ODM470 disdrometer	Optical disdrometer	Drop size distribution (1 min, size range: size, 128 size bins)	Time series of precipitation rate and type (rainfall, snow, mixed, and convective/stratiform), drop size distribution parameters, simulated radar moments at different frequencies (from S band to Ka band), and sea surface temperature (SST); salinity; evaporation $E$ ; freshwater budget ( $E - P$ ); sensible and latent heat fluxes; drag, latent heat, and sensible heat transfer coefficients; warm layer flag
<b>Aerosols and trace gases</b>			
CSIRO proton transfer reaction mass spectrometer (PTRMS)	Spectrometer measuring different trace gases in the lower troposphere	VOC atmospheric mixing ratios Dimethyl sulfide (DMS) mixing ratios	Time series of 5–10-min resolution of atmospheric VOC and DMS mixing ratios
CSIRO VOC sequencer	Absorption tubes measuring volatile organic compounds (VOC)	VOC atmospheric mixing ratios (carbonyls, aldehydes and ketones)	Daily time series of VOC atmospheric mixing ratios (carbonyls, aldehydes and ketones)
CSIRO condensation particle counter (TSI 3776)	Particle counter measuring condensation nuclei	Condensation nuclei (aerosol CN) number concentrations larger than 3 nm	Time series (1-s resolution) of CN number concentrations larger than 3 nm
CSIRO aerodynamic particle sizer (TSI 3320)	Device measuring number of particle per aerodynamic diameter	Particle number size distributions, 0.5–20 $\mu\text{m}$ (52 channels)	Time series (5-min resolution) of aerosol size distribution
CSIRO scanning mobility particle spectrometer (TSI SMPS, Long-DMA)	Spectrometer measuring number of particle per mobility diameter	Particle number size distributions, 14–700 nm (108 log-scale bins)	Time series (5-min resolution) of aerosol size distribution
CSIRO scanning mobility particle spectrometer (GRIMM, M-DMA)	Spectrometer measuring number of particle per mobility diameter	Particle number size distributions, 5–250 nm (64 bins per decade)	Time series (5-min resolution) of aerosol size distribution
CSIRO cloud condensation nuclei counter (DMT CCN-100)	Particle counter measuring cloud condensation nuclei number concentrations	CCN number concentrations ( $\text{cm}^{-3}$ )	Time series (1-s resolution) of CCN number concentration at 0.5% supersaturation
CSIRO time-of-flight Aerosol Chemical Speciation Monitor (Aerodyne)	Speciation monitor measuring aerosol chemical composition	Real-time aerosol chemical composition ( $0.1 < D_p < 1 \mu\text{m}$ )	Time series (10-min resolution) of aerosol chemical composition only available for the first 5 days
CSIRO MOUDI cascade impactor (MSP model 130 high flow impactor)	Impactor measuring size-resolved aerosol chemical composition	Size resolved aerosol chemical composition  Including soluble ions $\text{Na}^+$ , $\text{NH}_4^+$ , $\text{K}^+$ , $\text{Mg}_2^+$ , $\text{Ca}^+$ , $\text{F}^-$ , $\text{CH}_3\text{COO}^-$ , $\text{HCOO}^-$ , $\text{MSA}^-$ , $\text{Cl}^-$ , $\text{Br}^-$ , $\text{NO}_3^-$ , $\text{SO}_4^{2-}$ , $\text{C}_2\text{O}_4^{2-}$ , $\text{PO}_4^{3-}$	Weekly time series of size-resolved aerosol chemical composition with five size cuts at diameters 0.25, 0.44, 0.77, 1.4, and 2.5 $\mu\text{m}$

Table ES3. Continued.

Instrument name/operating organization	Instrument description	Primary measurement	Derived quantities
QUT volatility hygroscopicity tandem differential mobility analyzer (VH-TDMA)	Analyzer measuring aerosol hygroscopic growth and volatility factors	Aerosol hygroscopic growth factors and volatility at 250°C at $D_p = 40, 100,$ and 150 nm; raw resolution is 18 min; three sizes (bin width ~10% of $D_p$ )	Time series (1-h resolution) of aerosol hygroscopic growth factors and volatility at 250°C at $D_p = 40,$ 100, and 150 nm
QUT transmission electron microscopy grid sampling (TEM)	Electron microscope device measuring aerosol morphology and composition	Aerosol particle morphology and composition. Average sample length 20 h (range 6–30 h).	14 samples taken over the period (21 Mar–13 Apr 2016)
CSU continuous flow diffusion chamber (CFDC)	Diffusion chamber measuring INP number concentrations	Time series (1-s resolution) of INP number concentrations	Time series (10–15-min resolution) of INP number concentrations
CSU ice spectrometer (from filters)	Filters to collect ice nucleating particles	Ice nucleating particle number concentration and freezing temperature spectra	Analyzed ice nucleating particle number concentrations over 21–62 h
CSU Wideband Integrated Bioaerosol Spectrometer (WIBS-4A)	Fluorescence from single aerosol particles in three excitation/emission channels, and sizes of all particles	Numbers and sizes of fluorescent particles in three channels of 310–400, 420–650, and 420–650 nm, as well as number and size of total aerosol particles $> 0.8 \mu\text{m}$	Size distribution of total aerosols and fluorescent biological aerosol particles between 0.8 and 12 $\mu\text{m}$
CSIRO Multi-Angle Absorption Photometer (MAAP; Thermo Scientific 5012)	Photometer measuring black carbon concentration and aerosol absorption coefficient	Black carbon concentration and aerosol absorption coefficient (1-min resolution)	Time series (1-min resolution) of processed black carbon concentration and aerosol absorption coefficient
CSIRO polar nephelometer (Ecotech Aurora 4000)	Nephelometer measuring aerosol scattering coefficient	Aerosol scattering coefficient (1-s resolution)	Time series of aerosol scattering coefficient
CSIRO ozone monitor (2 $\times$ Thermo Scientific Model 49i analyzers)	Ozone monitor measuring ozone mixing ratio	Ozone mixing ratio (1-min resolution)	Time series (1-min resolution) of ozone mixing ratio
ANSTO 700L dual flow loop two-filter radon detector	Radon detector	Radon concentration	Time series (1-h resolution) radon concentration
CSIRO Picarro G2301	Device measuring the mixing ratio of different gases	$\text{CO}_2, \text{D}, \text{H}_2\text{O}$ mixing ratio [1-s (raw) resolution]	Time series (1-s resolution) of $\text{CO}_2, \text{D}, \text{H}_2\text{O}$ mixing ratio
CSIRO Aerodyne Mini-QCL	Device measuring the mixing ratio of different gases	$\text{N}_2\text{O}, \text{CO}, \text{H}_2\text{O}$ mixing ratio [1-s (raw) resolution]	Time series (1-s resolution) of $\text{N}_2\text{O}, \text{CO}, \text{H}_2\text{O}$ mixing ratio
<b>Underway ship baseline data</b>			
DGPS system providing position, attitude, velocity, acceleration and timing information  Seapath 330+ with Seatex MRU 5+ and FUGRO Seastar 3610 DGNSS receiver		Longitude, latitude, speed, course, heading, altitude above MSL	Processed time series of these parameters at 1-s, 10-s, 1-min, 5-min, and 10-min resolution
Axis Doppler log—measuring vessel speed through water  Kongsberg Maritime Skipper DL850		Longitudinal and transversal water and ground speeds	Processed time series of these parameters at 1-s, 10-s, 1-min, 5-min, and 10-min resolution
Thermosalinograph Remote T probe Fluorometer Underway pCO <sub>2</sub>	Various seawater instruments	Sea surface salinity and temperature, active phytoplankton biomass and Chl concentration, equilibrator water temperature, XCO <sub>2</sub> , water vapor, Licor pressure, equilibrator pressure	Processed time series of these parameters at 1-s, 10-s, 1-min, 5-min, and 10-min resolution
Vaisala T&RH HMT333 Vaisala Barometer RM Young Wind Sensor Type 05108 Gill WindObserver II Eppley PIR and PSP LI-COR LI-190 Quantum	Various meteorological instruments	Port and starboard: Air temperature, relative humidity, pressure, wind speed and direction (relative to ship and true), maximum wind gust, shortwave radiation (0.2–4 mm), longwave radiation (4–100 mm), photosynthetically active radiation (0.4–0.7 mm)	Processed time series of these parameters at 1-s, 10-s, 1-min, 5-min, and 10-min resolution

Table ES3. Continued.

Instrument name/operating organization	Instrument description	Primary measurement	Derived quantities
Air-sea interactions			
NOAA flux system Ultrasonic 3-axis anemometer (Gill Windmaster) Eppley PSP and PIR Vaisala/HMT335 Vaisala/PTB220 Floating thermistor (YSI46040, "sea snake") Optical rain gauge (ORG-815DA) Li-COR 7500 open path CO <sub>2</sub> /H <sub>2</sub> O analyzer Riegl laser altimeter	Various instruments	Longitude, latitude, wind speed and direction, shortwave and longwave radiation, SST, pressure, air temperature, relative humidity, rainfall rate	Time series (1 min), meteorological data: Longitude, latitude, wind speed and direction, shortwave and longwave radiation, SST, pressure, air temperature, relative humidity, rainfall rate Time series (5 min or 30 min), bulk model flux outputs and meteorological data: Longitude, latitude, wind speed and direction, shortwave and longwave radiation, SST, salinity, pressure, air temperature, specific humidity at 21.5 m and at sea surface, rainfall rate, wind stress, sensible and latent heat fluxes, rain heat flux, 10-m neutral wind speed, 10-m neutral drag coefficient Time series (10 min or 60 min), turbulent flux outputs and meteorological data: Same parameters as previous row; clear-sky shortwave and longwave radiation; sensible and latent heat fluxes (covariance and inertial dissipation); streamwise and cross-stream wind stress covariance; wind stress inertial dissipation; structure function parameters ( $ct^2$ , $cq^2$ , $cu^2$ , $cw^2$ ); standard deviation (std) of specific humidity; CO <sub>2</sub> concentration and std of concentration; 10-m neutral wind speed, air temperature and specific humidity Time series (10 min), wave spectra and wave statistics: Wave spectrum, significant wave height, mean zero crossing period, energy period, peak period, zeroth to fourth moments of the wave spectrum, peak frequency

Front south of 50°S and broadly in the 148°E region (Bharti et al. 2019). During the first period, cloud cover was dominated by open-cell stratocumulus and shallow scattered cumulus in regions of cold advection associated with a rapid succession of frontal passages. During the second period, there was a rapid evolution from shallow convection (deeper than in the first period) to extended areas of stratocumulus. Table ES4 lists the times and locations of five cases when the R/V *Investigator* passed through the cold sector of major cold fronts.

Although the instrumentation for CAPRICORN II was similar to that for CAPRICORN I, there were additions to the suite as listed in Table ES5. After departing Hobart on 11 January 2018, R/V *Investigator* passed south of 50°S on 18 January and south of 60°S on 28 January. A series of zonal transects between meridians of 150° and 132°E were then conducted north of the

**Table ES4.** Dates and approximate duration that the R/V *Investigator* was in the cold sector of major cold fronts during CAPRICORN I.

Date of cold sector (southerly or south- westerly flow)	Comments	Latitude (°) of ship during this flow	Longitude (°) of ship during this flow	Date and time of cold front	Latitude (°) of ship at frontal passage	Longitude (°) of ship at frontal passage
17 Mar	Ship in weak southwesterly flow	-46 to -47	141 to 142	1000 UTC 17 Mar	-47	142
29 Mar	Briefly in cold sector following passage of weak front, not far south of high pressure center	-50	145	2100 UTC 29 Mar	-50	145
5 Apr	Ship just north of deep low pressure system	-52 to -53	147	1500 UTC 5 Apr	-53	147
10 Apr	Weak cold front but clear and persistent southwesterly flow	-52	148	0800 UTC 10 Apr	-51	148
11 Apr	Another frontal passage, with little preceding northwesterly flow (cyclone center adjacent to Antarctica)	-51	151	1800 UTC 11 Apr	-51	151

**Table ES5.** List of instruments used in CAPRICORN II.

Instrument name/operating organization	Instrument description	Primary measurement	Derived quantities
<b>Clouds and precipitation</b>			
BoM W-band Cloud Radar (BASTA)	Vertically pointing 95-GHz cloud radar	Vertical profiles (12 s, 25 m) of calibrated 95-GHz radar reflectivity and Doppler velocity	Cloud mask, cloud fraction, thermodynamic phase (with lidar)
BoM lidar (RMAN-511)	Vertically pointing 355-nm cloud and aerosol backscatter lidar	Vertical profiles (2 min, 15 m) of calibrated lidar co-polar and cross- polar backscatter, depolarization ratio	Cloud mask, cloud fraction, thermodynamic phase (with cloud radar)
University of Melbourne lidar (miniMPL)	Vertically pointing 532-nm cloud and aerosol backscatter lidar	Vertical profiles (2 min, 15 m) of calibrated lidar co-polar and cross-polar backscatter, depolarization ratio	Cloud mask, cloud fraction, thermodynamic phase (with cloud radar)
University of Utah 2-channel microwave radiometer (MWR)	2-channel microwave radiometer	20.6- and 31.2-GHz brightness temperatures	Liquid water path, water vapor path
AAD Micro Rain Radar (MRR-PRO)	Vertically pointing 24-GHz rain radar	Vertical profiles (10 s, 35 m) of 24-GHz radar reflectivity, Doppler velocity, and spectral width	Vertical profiles of precipitation rate, DSD parameters
NCAR 915-MHz wind profiler	Vertically pointing wind profiler measuring 915-MHz reflectivity and the three wind components	Vertical profiles of radar reflectivity and three-dimensional wind components	Vertical profiles of precipitation frequency of occurrence, precipitation fraction, 3D winds
NCAR zenith wind lidar	Vertically pointing Doppler lidar measuring vertical motions	Vertical profiles of vertical wind (horizontal winds uncorrected)	Vertical profiles of cloud frequency of occurrence, cloud fraction, 3D winds
NCAR lidar ceilometer	Vertically pointing ceilometer measuring cloud base and backscatter profiles	Cloud and aerosol layer detection and vertical profiles (lidar backscatter)	Time series of cloud layer detection

Table ES5. Continued.

Instrument name/operating organization	Instrument description	Primary measurement	Derived quantities
University of Hamburg ODM470 disdrometer	Optical disdrometer	Drop size distribution (1 min, size range: size, 128 size bins)	Time series of precipitation rate and type (rainfall, snow, mixed, and convective/stratiform), drop size distribution parameters, simulated radar moments at different frequencies (from S band to Ka band), and sea surface temperature (SST); salinity; evaporation $E$ ; freshwater budget ( $E - P$ ); sensible and latent heat fluxes; drag, latent heat, and sensible heat transfer coefficients; warm layer flag
<b>Aerosols and trace gases</b>			
NASA/CSIRO Microtops sunphotometer	Sunphotometer measuring aerosol optical depth on demand (needs cloud-free conditions)	Aerosol optical depth in noncloudy air	Manual spot measurements of aerosol optical depth
CSIRO condensation particle counters (TSI 3776 and 3772)	Particle counter measuring condensation nuclei	Condensation nuclei (aerosol) number concentrations larger than 3 nm and larger than 10 nm	Time series (1-s resolution) of CN number concentrations larger than 3 nm and larger than 10 nm
CSIRO aerodynamic particle sizer (TSI 3320)	Device measuring number of particle per aerodynamic diameter	Particle number size distributions, 0.5–20 $\mu\text{m}$ (52 channels)	Time series (1-min resolution) of aerosol size distribution
CSIRO scanning mobility particle spectrometer (TSI SMPS, Long-DMA)	Spectrometer measuring number of particle per mobility diameter	Particle number size distributions, 14–700 nm (108 log-scale bins)	Time series (5-min resolution) of aerosol size distribution
CSIRO scanning mobility particle spectrometer (GRIMM, M-DMA)	Spectrometer measuring number of particle per mobility diameter	Particle number size distributions, 5–250 nm (64 bins per decade)	Time series (5-min resolution) of aerosol size distribution
CSIRO cloud condensation nuclei counter (DMT CCN-100)	Particle counter measuring cloud condensation nuclei number concentrations	CCN number concentrations ( $\text{cm}^{-3}$ )	Time series (1-h resolution) of CCN number concentration at supersaturations of 0.2%, 0.3%, 0.4%, 0.5%, 0.6%, 1.0%
CSIRO time-of-flight Aerosol Chemical Speciation Monitor (Aerodyne)	Speciation monitor measuring aerosol chemical composition	Real-time aerosol chemical composition ( $0.1 < D_p < 1 \mu\text{m}$ )	Time series (10-min resolution) of aerosol chemical composition
CSIRO PM1 filter sampler	Sampler measuring submicron aerosol chemical composition	Aerosol chemical composition Including soluble ions $\text{Na}^+$ , $\text{NH}_4^+$ , $\text{K}^+$ , $\text{Mg}_2^+$ , $\text{Ca}^+$ , $\text{F}^-$ , $\text{CH}_3\text{COO}^-$ , $\text{HCOO}^-$ , $\text{MSA}^-$ , $\text{Cl}^-$ , $\text{Br}^-$ , $\text{NO}_3^-$ , $\text{SO}_4^{2-}$ , $\text{C}_2\text{O}_4^{2-}$ , $\text{PO}_4^{3-}$	Daily time series of submicron aerosol chemical composition
QUT volatility hygroscopicity tandem differential mobility analyzer (VH-TDMA)	Analyzer measuring aerosol hygroscopic growth and volatility factors	Aerosol hygroscopic growth factors and volatility at 250°C at $D_p = 40, 100$ , and 150 nm; raw resolution is 18 min; three sizes (bin width ~10% of $D_p$ )	Time series (1-h resolution) of aerosol hygroscopic growth factors and volatility at 250°C at $D_p = 40, 100$ , and 150 nm
QUT chemical ionization mass spectrometer (CIMS)	Mass spectrometer measuring gas phase properties	Concentration of gas phase VOCs, sulfuric acid, and MSA	Time series of gas phase VOCs, sulfuric acid, and MSA concentrations
CSU continuous flow diffusion chamber (CFDC)	Diffusion chamber measuring INP number concentrations	Time series (1-s resolution) of INP number concentrations	Time series (5–20-min resolution) of INP number concentrations
CSU ice spectrometer (from filters)	Filters to collect ice nucleating particles; equivalent filters collected for sequencing	Ice nucleating particle number concentration freezing temperature spectra	Analyzed ice nucleating particle number concentrations over 21–62 h
CSU aerosol filters	Filters for bioaerosol (bacterial) analyses	Next-generation sequencing analyses	Bacterial biodiversity characterization over 21–62 h
NOAA Wideband Integrated Bioaerosol Spectrometer (WIBS-4A)	Fluorescence from single aerosol particles in three excitation/emission channels, and sizes of all particles	Numbers and sizes of fluorescent particles in three channels of 310–400, 420–650, and 420–650 nm, as well as number and size of total aerosol particles $> 0.8 \mu\text{m}$	Size distribution of total aerosols and fluorescent biological aerosol particles between 0.8 and 12 $\mu\text{m}$

Table ES5. Continued.

Instrument name/operating organization	Instrument description	Primary measurement	Derived quantities
CSIRO polar nephelometer (Ecotech Aurora 4000)	Nephelometer measuring aerosol scattering coefficient	Aerosol scattering coefficient (1-s resolution)	Time series (1 s) of aerosol scattering coefficient
CSIRO ozone monitor (2 × Thermo Scientific Model 49i analyzers)	Ozone monitor measuring ozone mixing ratio	Ozone mixing ratio (1-min resolution)	Time series (1-min resolution) of ozone mixing ratio
ANSTO 700L dual flow loop two-filter radon detector	Radon detector	Radon concentration	Time series (1-h resolution) radon concentration
CSIRO Picarro G2301	Device measuring the mixing ratio of different gases	CO <sub>2</sub> , CH <sub>4</sub> , H <sub>2</sub> O mixing ratio [1-s (raw) resolution]	Time series (1-s resolution) of CO <sub>2</sub> , D, H <sub>2</sub> O mixing ratio
CSIRO Aerodyne Mini-QCL	Device measuring the mixing ratio of different gases	N <sub>2</sub> O, CO, H <sub>2</sub> O mixing ratio [1-s (raw) resolution]	Time series (1-s resolution) of N <sub>2</sub> O, CO, H <sub>2</sub> O mixing ratio
University of Wollongong Multiaxis Differential Optical Absorption Spectrometer (MAX-DOAS)	Solar spectrometer measuring aerosol and trace gas vertical profiles in the bottom 4 km of the atmosphere	HCHO, CHOCHO, O <sub>3</sub> , N <sub>2</sub> O, and aerosol vertical profiles [10-Hz (raw) resolution]	Time series (1 h) of vertical profiles of trace gases and aerosols
<b>Underway ship baseline data</b>			
DGPS system providing position, attitude, velocity, acceleration and timing information  Seapath 330+ with Seatek MRU 5+ and FUGRO Seastar 3610 DGNSS receiver		Longitude, latitude, speed, course, heading, altitude above MSL	Processed time series of these parameters at 1-s, 10-s, 1-min, 5-min, and 10-min resolution
Axis Doppler log—measuring vessel speed through water  Kongsberg Maritime Skipper DL850		Longitudinal and transversal water and ground speeds	Processed time series of these parameters at 1-s, 10-s, 1-min, 5-min, and 10-min resolution
Thermosalinograph Remote T probe Fluorometer Underway pCO <sub>2</sub>	Various seawater instruments	Sea surface salinity and temperature, active phytoplankton biomass and Chl concentration, equilibrator water temperature, XCO <sub>2</sub> , water vapor, Licor pressure, equilibrator pressure	Processed time series of these parameters at 1-s, 10-s, 1-min, 5-min, and 10-min resolution
Vaisala T&RH HMT333 Vaisala Barometer RM Young Wind Sensor Type 05108 Gill WindObserver II Eppley PIR and PSP LI-COR LI-190 Quantum	Various meteorological instruments	Port and starboard: Air temperature, relative humidity, pressure, wind speed and direction (relative to ship and true), maximum wind gust, shortwave radiation (0.2–4 mm), longwave radiation (4–100 mm), photosynthetically active radiation (0.4–0.7 mm)	Processed time series of these parameters at 1-s, 10-s, 1-min, 5-min, and 10-min resolution
<b>Air-sea interactions</b>			
BoM/IMOS Thermosalinograph Vaisala T&RH (HMT333), Vaisala Barometer RM Young Wind Sensor (05108), Gill WindObserver II Eppley PIR and PSP RM Young siphon rain gauge (50202)	Various meteorological instruments	Longitude, latitude, wind speed and direction, shortwave and longwave radiation, bulk SST, air pressure, air temperature, relative humidity, rainfall rate, wind stress, sensible and latent heat fluxes, rain heat flux, 10-m neutral wind speed, 1.5- and 2-m calculated relative humidity, 1.5- and 2-m calculated air temperature, net heat flux, SST skin, mass flux, longwave radiation net, shortwave radiation net	Time series (1 min), bulk model flux outputs and met data:  Longitude, latitude, wind speed and direction, shortwave and longwave radiation, bulk SST, air pressure, air temperature, relative humidity, rainfall rate, wind stress, sensible and latent heat fluxes, rain heat flux, 10-m neutral wind speed, 1.5- and 2-m calculated relative humidity, 1.5- and 2-m calculated air temperature, net heat flux, SST skin, mass flux, longwave radiation net, shortwave radiation net

sea ice and the ship returned north of 60°S on 15 February and north of 50°S on 20 February. Thus, the R/V *Investigator* spent approximately 9 days north of 50°S, 12 days between 60° and 50°S, and 18 days south of 60°S. Cases of special meteorological interest are listed in the next two tables. Table ES6 describes the time periods of collocated GPM observations when rain, snow, or mixed-phase precipitation was present as these cases will be useful for satellite evaluation studies. Table ES7 identifies the time period and duration of incidents when the R/V *Investigator* traversed cold sectors or cold fronts. Note that CAPRICORN II was coordinated with SOCRATES as there were four G-V passes over the R/V *Investigator* (22 January, 23 January, 25 January, 17 February 2018) Of these, the 17 February flight provided the best collaborative measurements with the NCAR G-V conducting multiple passes of the R/V *Investigator* below, within, and above a supercooled stratocumulus overcast.

The CAPRICORN II track was largely determined by oceanographic objectives. The ship would remain stationary from 6 to 24 h, then move approximately 50 km to the next site. Thus, weather systems that passed on time scales of a few days were well sampled almost as if from a stationary platform, while the latitudinal variations of the large-scale atmosphere were characterized over a period of weeks. A contoured frequency by altitude (CFAD) diagram shows statistical distributions of a quantity as a function of height, where the contours give the frequency of occurrence of a quantity at a given altitude in the atmosphere. CFADs of W-band cloud radar reflectivity are shown in Fig. ES1 separated by latitude band for the full troposphere and for layers within the BL. For the W band, a -20 dBZ or less is nonprecipitating, a threshold of about -15 dBZ is associated with drizzle production, 0 dBZ represents heavy drizzle/light rain, and moderate rain is usually associated with reflectivity > 20 dBZ. A trend of increasing cloud occurrence from north to south was found even as the depth of the layer over which clouds were observed contracted as the tropopause lowered. The deep CFADs demonstrate the tendency for more precipitation in the southern latitudes where it was mostly realized as snow. Clouds below 2 km were predominantly at all latitudes and

**Table ES6. GPM overpasses of the R/V Investigator during CAPRICORN II when precipitation was observed at the location of the ship. In total there were 56 passes of the GPM core satellite where the subsatellite track passed within 300 km of the R/V *Investigator*.**

Time	Orbit	Distance (km)	Latitude (°)	Longitude (°)	Precipitation at ship
1400 UTC 18 Jan 2018	22105	299.94	-50.40	143.53	Rain showers
2000 UTC 22 Jan 2018	22172	124.76	-54.53	141.33	Rain showers
1900 UTC 25 Jan 2018	22218	87.65	-58.85	139.84	Stratiform rain
1300 UTC 26 Jan 2018	22229	12.84	-59.35	139.85	Stratiform snow
1300 UTC 28 Jan 2018	22260	60.11	-61.85	139.85	Stratiform snow
1400 UTC 29 Jan 2018	22276	83.44	-63.35	139.83	Snow showers
1500 UTC 29 Jan 2018	22278	178.74	-63.35	139.83	Snow showers
1300 UTC 30 Jan 2018	22291	150.95	-64.21	139.83	Stratiform snow
1100 UTC 7 Feb 2018	22414	110.98	-63.05	146.45	Stratiform snow
1300 UTC 8 Feb 2018	22432	161.02	-62.58	142.05	Stratiform rain
1100 UTC 9 Feb 2018	22445	177.39	-62.17	138.41	Snow showers
1000 UTC 12 Feb 2018	22491	219.76	-64.45	132.08	Stratiform snow
1300 UTC 12 Feb 2018	22494	74.44	-64.45	132.08	Stratiform snow
1000 UTC 13 Feb 2018	22507	171.02	-63.00	132.11	Snow showers
1300 UTC 15 Feb 2018	22541	71.1	-58.97	132.03	Rain showers
0800 UTC 16 Feb 2018	22552	121.95	-57.52	132.00	Drizzle
0700 UTC 17 Feb 2018	22567	47.93	-56.77	136.97	Snow showers

**Table ES7.** List of time periods and duration of incidents when the R/V *Investigator* traversed cold sectors or cold fronts during CAPRICORN II. It is worth noting that fewer cold fronts were passed underneath for CAPRICORN II (compared with CAPRICORN I and MARCUS), because a large amount of time was spent in the high-latitude Southern Ocean region.

Date of cold sector (southerly or southwesterly flow)	Comments	Latitude ( $^{\circ}$ ) of ship during this flow	Longitude ( $^{\circ}$ ) of ship during this flow	Date and time of cold front	Latitude ( $^{\circ}$ ) of ship at frontal passage	Longitude ( $^{\circ}$ ) of ship at frontal passage
14 Jan	Just south of Hobart, weak cold front	-46 to -47	146	0900 UTC 14 Jan	-46	146
18 Jan	Developing low pressure to the south	-50 to -51	144	1700 UTC 18 Jan	-51	143
23 Jan	Ship passes west of a weak low pressure, flow turns weakly southerly/southwesterly	-55	141			
26 Jan	Ship located to the west of low pressure center no fronts	-59	140			
28–29 Jan	Ship passes close to center of deep low, then experiences southerly winds as low propagates eastward	-62	140			
31 Jan	Ship near the ice-free Antarctic coastline, weak low pressure to the north, near-surface southerly winds off the continent	-65	140			
4–5 Feb	Ship west of a deep low pressure with near-surface southerly winds off the continent	-65	150			
14–15 Feb	Ship located southwest of a deep low	-61 to -59	132			
16–18 Feb	Southerly–southwesterly flow around a very weak low, located east of the ship	-57	132–141			

were mostly nonprecipitating north of 50°S. The sea surface temperatures (SSTs) north of the subantarctic oceanic front (Armour et al. 2016) were above normal with an  $\sim +1.5^{\circ}\text{C}$  anomaly in the Tasman Sea associated with a seasonal atmospheric blocking pattern (Salinger et al. 2019). South of 50°S high clouds above 6 km were infrequent. The BL clouds (Fig. ES1d) increased in altitude as the BL deepened south of 50°S and there is evidence for light precipitation that often did not extend to the surface. South of 60°S, the occurrence of precipitation from deep cloud systems is notable. The more frequent BL clouds and associated precipitation south of 60°S in Fig. ES1f extend closer to the surface than in the more northern latitudes and a light precipitation mode near  $-10 \text{ dBZ}_e$  is also more prominent.

Instrumentation installed on the AA for the MARCUS campaign is summarized in Table ES8. The majority of the instrumentation worked well for most of the campaign with a couple of exceptions: the three-channel microwave radiometer never operated so is not included in Table ES8; the polarization channel on the Micropulse Lidar (MPL) was not operable until 13 January 2018 so depolarization measurements are only available after that; and the stabilized platform worked sporadically. Because some of the other zenith-pointing measurements were not mounted on a stabilized platform, information from the ship navigation system is

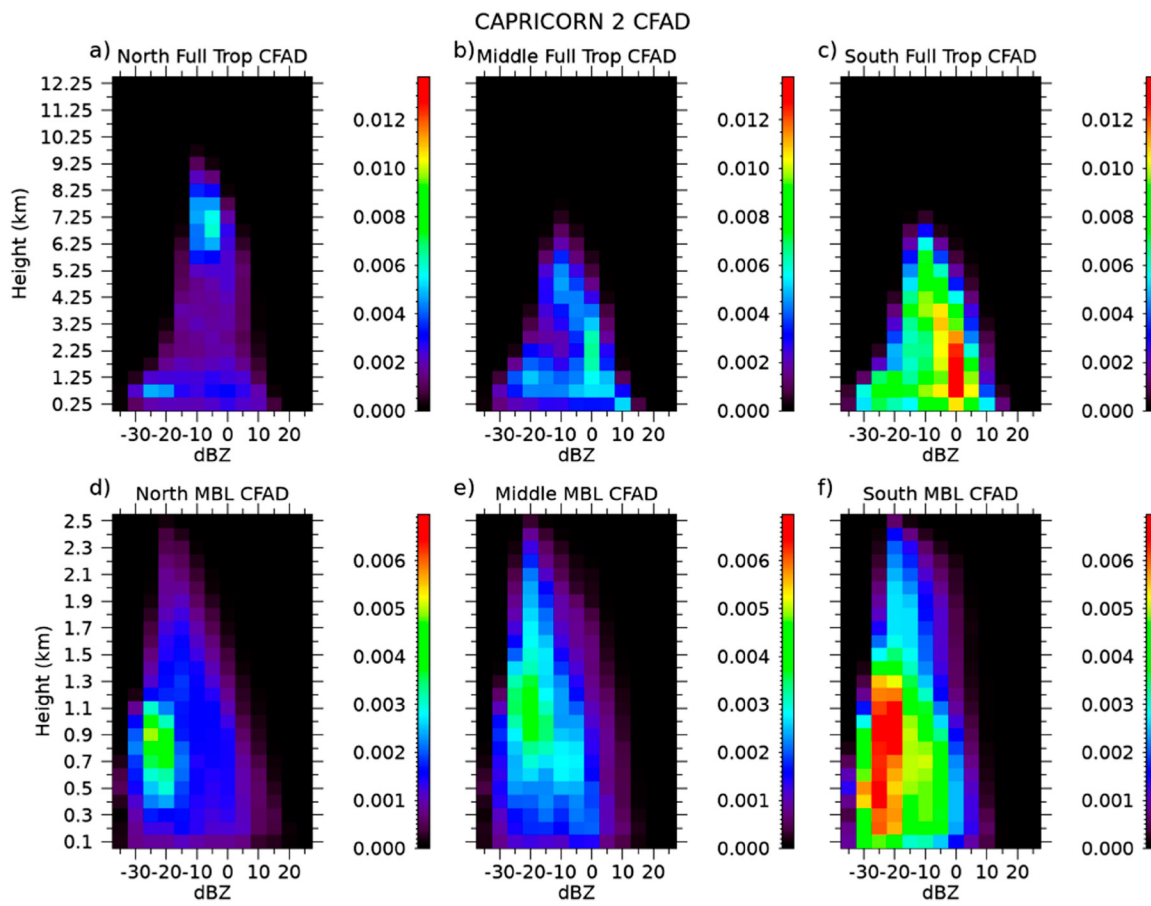


**Fig. ES1.** Contour frequency by altitude diagram (CFAD) analysis from the vertically pointing W-band radar on the R/V *Investigator* during CAPRICORN II. (a)–(c) The full vertical depth of the measurements where normalization is by the total number of hydrometeor observations summed from (a) to (c). (d)–(f) Frequencies from layers that are fully contained below 2.5 km where normalization is by the total number of observations summed across (d)–(f). “North” in (a) and (d) are for latitudes north of 50°S, “Middle” in (b) and (e) show latitudes between 50° and 60°S, and “South” in (c) and (f) show latitudes south of 60°S.

**Table ES8.** Instrumentation installed on the AA for the MARCUS (unless specified, DOE ARM was the operating organization of the probe).

Instrument name/operating organization	Instrument description	Primary measurement	Derived quantities
Atmosphere Emitted Radiance Interferometer (AERI)	Passive remote sensing device	Downwelling infrared reliance from Earth's atmosphere	Derived quantities include atmospheric moisture and temperature, as well as cloud properties
ARM Aerosol Observing System (AOS)	Number of instruments measuring aerosol physical and optical properties	Numbers of aerosols, sizes of aerosols, particle sizes	Absorption, concentration, size distributions, scattering
CCN particle counter	Draws air sample through column with supersaturated water vapor	Number of particles activated into cloud drops as function of supersaturation	Concentration of cloud condensation nuclei
Ceilometer	Remote sensing instrument transmitting and receiving infrared light pulses	Receiver detects amount of light scattered by clouds and precipitation	Cloud height, vertical visibility, and planetary boundary layer height
Cimel sun photometer	Multichannel automatic sun- and sky-scanning radiometer	Direct solar irradiance and sky radiance at Earth's surface	Aerosol optical depth or cloud optical dept
CO analyzer	Measures trace gas concentration through infrared radiation	Absorption of infrared radiation at 4.6 $\mu$ m	Concentration of CO in parts per billion by volume dry air

Table ES8. Continued.

Instrument name/operating organization	Instrument description	Primary measurement	Derived quantities
Humidified tandem differential mobility analyzer (H-TDMA)	Part of AOS measuring how aerosol particles grow or shrink when exposed to varying relative humidity	One differential mobility analyzer (DMA) selects narrow size range of aerosols, which exposed to varying relative humidity by humidification system and measured by second DMA	Concentration, particle size distribution, humidification factor
Infrared thermometer	Pyrometer	Measures equivalent blackbody brightness temperature	Surface skin temperature
Laser disdrometer	Laser optical device for measuring raindrop size and fall speed	Fall speed and size of raindrops	Raindrop size distribution, precipitation rate, radar reflectivity
Marine precipitation instrumentation	Rain gauge	Rainfall accumulated as a function of time	Rainfall rate, total precipitation
Marine W-band (95 GHz) Cloud Radar	Active remote sensing cloud radar	Radar reflectivity and Doppler velocity	Cloud heights and microphysical retrievals
AAD Micro Rain Radar (MRR-PRO)	Vertically pointing 24-GHz rain radar	Vertical profiles (10 s, 35 m) of 24-GHz radar reflectivity, Doppler velocity, and spectral width	Vertical profiles of precipitation rate, DSD parameters
Micropulse lidar	Active ground-based sensor transmitting and receiving pulses of radiation at 532 nm	Backscatter return and polarization	Height of aerosol and cloud layers and derived quantities (optical depth, phase, particle size, etc.)
Microwave radiometer (2-channel)	Sensitive microwave receiver that measures radiance at 23.8 and 31.4 GHz	Brightness temperature at two frequencies	Column integrated liquid water and water vapor
Navigational location and attitude	Several instruments measuring ship current position and attitude	Latitude, longitude, roll, pitch and yaw angles	Used for postdeployment processing or instrument data
Nephelometer	Part of AOS measuring total scattering and hemispheric backscattering of aerosols	Pair measuring scattering at ambient conditions and another as function of slowly increasing or decreasing humidity	Hygroscopic growth factor as function of relative humidity
O <sub>3</sub> monitor	Part of AOS using ultraviolet photometry in dual absorption cell	O <sub>3</sub> concentration by	
Particle soot absorption photometer	Part of AOS, collects particles on a substrate	Changes in light transmission relative to reference filter	Aerosol absorption and extinction
Radar wind profiler	Acoustic sounding system	Backscattered signal strength between 0.1 and 5 km	Wind profiles, virtual temperature profiles
Rain gauge siphon	Receptacle to collect and measure precipitation	Rainwater gathered in interval of time	Rainfall rate and total precipitation
Rain gauge optical	Optical rain gauge to collect and measure precipitation	Rainwater gathered in interval of time	Rainfall rate and total
Rotating shadowband spectroradiometer	Similar to MFRSR using automated shadowbanding technique	Spectrally resolved direct-normal, diffuse-horizontal and global-horizontal irradiance between 360 and 1,070 nm	Shortwave spectral irradiance (diffuse downwelling, direct normal and total downwelling)
Skyrad radiometers	Collection of radiometers	Downwelling broadband shortwave and longwave irradiance	Cloud fraction as well as irradiances
Sounding system (balloonborne)	6-h balloonborne radiosonde system	Temperature, pressure, dewpoint, wind speed and direction	Vertical profiles of temperature, pressure, dewpoint, wind speed and direction
Stabilized platform	Platform to keep W-band radar zenith pointing	Position of table	If not working, its position can be used to correct radar data
Total sky imager	Provides hemispheric sky images during day	Time series of sky images	Fraction of sky view covered by clouds
Ultra High Sensitivity Aerosol Spectrometer (UHSAS)	Laser based aerosol particle spectrometer system	Number of aerosol particles in size bins between 60 and 1,000 nm	Aerosol concentration and aerosol size distribution

Table ES8. Continued.

Instrument name/operating organization	Instrument description	Primary measurement	Derived quantities
KIT Wideband Integrated Bioaerosol Sensor (WIBS-4)	Fluorescence from single aerosol particles in three excitation/emission channels, and sizes of all particles	Numbers and sizes of fluorescent particles in three channels of 310–400, 420–650, and 420–650 nm, as well as number and size of total aerosol particles $> 0.8 \mu\text{m}$	Size distribution of total aerosols and fluorescent biological aerosol particles between 0.8 and 12 $\mu\text{m}$
CSU ice spectrometer (from filters)	Filters to collect ice nucleating particles	Ice nucleating particle number concentration freezing temperature spectra	Ice nucleating particle number concentrations over 24–48 h

being combined with the remote sensing measurements to provide the best estimate of the vertically pointing fields in a value added product.

A range of meteorological conditions were sampled, though it should be noted that the ship avoided strong cyclones for obvious reasons. Of particular interest is the amount of data collected in the cold sector of the cyclones, where disagreement between observed and modeled radiative fluxes often occurs. Using surface pressure fields from ERA5 and calculating the position of cold fronts following Simmonds et al. (2012), it was determined that there were 12 occasions on which a cold frontal zone was sampled, including 7 occurrences of the AA passing through identifiable cold fronts (Table ES9). Other notable meteorological events noted included a cyclone on 10 November 2017 near the sea ice edge that the AA passed underneath, full temporal sampling of coastal Antarctic cyclones while the ship was stationed

Table ES9. Time periods when the AA was in the cold sector (top) or passed through a cold frontal zone (bottom).

Date and time of cold sector (southerly or southwesterly flow)	Comments	Latitude ( $^{\circ}$ ) of ship	Longitude ( $^{\circ}$ ) of ship
2–3 Nov	Ship in southwesterly flow	–47 to –49	130 to 136
7 Nov	Briefly in cold sector following passage of weak front	–55	108 to 109
10 Nov	Ship passed beneath deep low pressure system centered around 65°S	–61 to –63	94 to 85
25–26 Nov	Ship heading northward, did not pass beneath cold front	–57 to –58	102 to 108
29 Nov	Briefly in southwesterly flow following a front	–50	130
16 Dec	In post-frontal airstream	–53 to –55	136 to 141
18 Jan	Briefly in southwesterly flow	–51 to –52	135 to 136
25 Jan	Ship around 65°S, in southerly airstream	–63 to –65	83 to 91
24–25 Feb	In post-frontal airstream	–53 to –57	95 to 107
10–11 Mar	In post-frontal airstream	–50 to –52	153 to 156
12 Mar	In post-frontal airstream while at Macquarie Island	–55	159
15 Mar	In post-frontal airstream while at Macquarie Island	–55	159

Date and time of cold front	Latitude ( $^{\circ}$ ) of ship	Longitude ( $^{\circ}$ ) of ship
0600 UTC 2 Nov	–47	136
0900 UTC 7 Nov	–55	109
0900 UTC 29 Nov	–50	130
0900 UTC 18 Jan	–51	136
1800 UTC 10 Mar	–50	153
0300 UTC 15 Mar	–55	159
0000 UTC 20 Mar	–55	159

at all three Antarctic bases (i.e., cyclones at Mawson on 11–13 February and 14–16 February, low-level precipitating SLW cloud layers regularly observed at Casey between 30 December 2017 and 5 January 2018, midlevel precipitating SLW clouds at Davis on 18–19 November 2017, and frontal passages when the ship was at Macquarie Island in mid-March 2018).

Table ES10 lists the instrumentation that was installed on the NSF–NCAR G-V aircraft during SOCRATES. This included (i) in situ cloud probes [Cloud Droplet Probe (CDP), Two-Dimensional Stereo Probe (2DS), Particle Habit Imaging and Polar Scattering probe (PHIPS), Two-Dimensional Cloud Probe (2DC), Precipitation Imaging Probe (PIP)] to measure cloud

**Table ES10. Instrumentation installed on NSF–NCAR G-V aircraft during SOCRATES.**

Instrument name	Instrument description	Primary measurement	Derived quantities
<b>In situ cloud probes</b>			
Two-Dimensional Stereo Probe (2D-S)	Optical array probe with 10- $\mu\text{m}$ resolution with horizontal and vertically oriented arrays ( $D$ 10–1,280 $\mu\text{m}$ nominally)	Cloud particle images and timing in sample volume	Number distribution function, nominally between 10 and 1,280 $\mu\text{m}$ and particle images from which other parameters can be derived ( $N$ , TWC, etc.)
Two-Dimensional Cloud Probe (2DC)	Cloud optical array imaging probe 25 $\mu\text{m}$ resolution (25–1,600 $\mu\text{m}$ )	Cloud particle images and timing in sample volume	Number distribution function, nominally between 25 and 1,600 $\mu\text{m}$ and particle images from which other parameters can be derived ( $N$ , TWC, etc.)
Closed Path Laser Hygrometer 2 (CLH2)	Infrared absorption of evaporated cloud particles and water vapor at 1.37 mm	Total water content	Total water content and condensed water content
Cloud Droplet Probe (CDP)	Forward scattering probe (2–50 $\mu\text{m}$ , ~2- $\mu\text{m}$ resolution)	Cloud particle size distribution	Liquid water content, effective radius other parameters
Counterflow Virtual Impactor (CVI)	Particles larger than threshold impacted into dry air and evaporated	Mass of evaporated cloud particles from hygrometer	Condensed water content
Particle Habit Imaging and Polar Scattering Probe (PHIPS HALO)	Two stereomicroscopic cameras and detectors for measuring scattering of light	Particle images and angular light scattering function	Size distributions, phase discrimination, asymmetry parameter, total concentrations
Precipitation Imaging Probe (PIP)	Precipitation optical array imaging probe 100- $\mu\text{m}$ resolution (100–6,400 $\mu\text{m}$ )	Precipitation particle size distribution	Number distribution function, nominally between 100 and 6,400 $\mu\text{m}$ ; no particle image data acquired during SOCRATES
Rosemount Icing Detector (RICE)	Vibrating wire on which supercooled water accretes	Voltage change	Periods with supercooled water
<b>Remote sensors</b>			
HIAPER Cloud Radar (HCR)	W-band radar on right wing of G-V, pointing nadir or zenith	Radar reflectivity, Doppler velocity	Profiles of reflectivity and velocity, cloud-top heights
High Spectral Resolution Lidar (HSRL)	532-nm 300-mW zenith pointing lidar	Backscatter coefficient and linear depolarization ratio	Cloud-top heights and phase
<b>Aerosols in situ</b>			
Automatic Giant Nuclei Impactor (AutoGNI)	Free-stream impaction on polycarbonate slides	Sizes and numbers of giant aerosol particles	Size distributions of giant aerosol particles
CCN counter	Measures CCN at constant supersaturation and variable supersaturation	Number of particles activated into cloud drops as function of supersaturation	CCN concentration as function of relative humidity
CN counter	Butanol-based aerosol counter	Concentration of aerosol particles condensed when exposed	Total concentration of aerosols with $D > \sim 11 \text{ nm}$
Continuous flow diffusion chamber	Diffusion chamber measuring INPs	Time series of INP concentrations	Integrated INP concentrations at varying resolutions
CSU ice spectrometer (from filters)	Filters to collect ice nucleating particles	Ice nucleating particle number concentration freezing temperature spectra.	Ice nucleating particle number concentrations over 20–60 min

Table ES10. Continued.

Instrument name	Instrument description	Primary measurement	Derived quantities
CVI inlet for aerosol collection	Titanium inlet for collecting particles on carbon-coated nickel grids or silicon nitride windows stored frozen for subsequent analysis	Composition of aerosol and cloud residuals measured by transmission electron microscopy and X-ray spectroscopy	Elemental inorganic composition of individual aerosol particles
UHSAS	Laser based aerosol particle spectrometer system	Number of aerosol particles in size bins between 0.06 and 1 $\mu\text{m}$	Aerosol concentration and aerosol size distribution
CSU Wideband Integrated Bioaerosol Spectrometer (WIBS-4A)	Fluorescence from single aerosol particles in three excitation/emission channels, and sizes of all particles	Numbers and sizes of fluorescent particles in three channels of 310–400, 420–650, and 420–650 nm, as well as number and size of total aerosol particles $> 0.8 \mu\text{m}$	Size distribution of total aerosols and fluorescent biological aerosol particles between 0.8 and 12 $\mu\text{m}$
<b>State parameters and other probes</b>			
Dropsondes	NCAR AVAPS Airborne Vertical Atmospheric Profiling Systems Vaisala module (RSS903)	Temperature, pressure and humidity	Vertical profiles of temperature, pressure, and humidity
Forward facing camera	Point Gray Research Hi-Res Flea H-Color 1–024 $\times$ 768 resolution camera	Forward facing images	Icing conditions
Gust probe	Gust system sensing pressure differences among ports placed in forward radome	High-resolution pressure, temperature, and vertical velocity	Temperature, pressure, and vertical velocity at varying resolutions
Longwave broadband radiometer	Kipp and Zonen CGR4	Irradiance in the 4.2–45- $\mu\text{m}$ spectral region	Longwave irradiance
Solar broadband radiometer	Kipp and Zonen CMP22	Irradiance in the 0.2–3.6- $\mu\text{m}$ spectral region	Solar broadband irradiance
Radiation pyrometer	Wintronics KT.19–85	Spectral radiance in the 9.5–11- $\mu\text{m}$ spectral region	Radiometric surface and cloud-top temperature
Vertical Cavity Surface Emitting Laser Hygrometer (VCSEL)	Open-path laser-based hygrometer measuring water vapor	Water vapor concentrations	Water vapor concentrations at varying resolutions

and precipitation particle size distributions, bulk water content probes [Counterflow Virtual Impactor (CVI), Closed Path Laser Hygrometer (CLH2), King probe] and probes to enable determination of particle phase (PHIPS, Rosemount icing detector) and to a lesser degree habit (PHIPS, 2DS, 2DC); (ii) the W-band HIAPER Cloud Radar (HCR; Vivekanandan et al. 2015) to provide measurements of 95-GHz reflectivity, Doppler velocity and spectra; (iii) a High Spectral Resolution Lidar (HSRL; Eloranta 2005) to measure the backscatter coefficient, extinction and linear depolarization; (iv) in situ aerosol probes [Ultra High Sensitivity Aerosol Spectrometer (UHSAS), Auto Giant Nuclei Impactor (GNI) for giant aerosols], inlet-based aerosol measurements including a condensation nuclei (CN) counter, two miniature CCN counters at fixed and variable supersaturation, a continuous flow diffusion chamber (CFDC) and a filter collection system for online and offline INP measurements, a second UHSAS and a WIBS-4A for fluorescent bioaerosol measurements that sampled from the CVI inlet; and (v) particle collection to provide information on the chemical composition of aerosols based on transmission electron microscopy with EDX for particles  $> 0.1\text{-}\mu\text{m}$  diameter, and scanning transmission X-ray microscopy by near-edge X-ray absorption fine structure (STXM-NEXAFS) analysis for particles  $> 0.1\text{-}\mu\text{m}$  diameter.

Data from the in situ cloud probes were first analyzed individually using dedicated analysis software to get probe-specific PSDs and number concentrations (Waitz et al. 2020, manuscript submitted to *Atmos. Meas. Tech.*; McFarquhar et al. 2017). Previous publications summarize well the manner in which the CDP, 2DC, and 2DS operate (Baumgardner et al.

2017; Lawson et al. 2006) and the methodology and caveats associated with the processing (McFarquhar et al. 2017). The processing of the PHIPS is described here and can also be found in Abdelmonem et al. (2016) and Schnaiter et al. (2018). The optical resolution of the stereo-microscopic images of individual cloud particles acquired by the PHIPS depends on the used magnification of the telescopic systems. During SOCRATES the microscopic imager was operated with  $6\times$  or  $4\times$  magnifications, which corresponds to optical resolutions of 3 and  $4\text{ }\mu\text{m}$ , respectively. Additionally, the instrument recorded the angular light scattering function of individual cloud particles at a wavelength of 532 nm, which can be used to estimate the ice particle asymmetry parameter. The shape of the angular light scattering function can also be exploited to discriminate between spherical and aspherical cloud particles with a high confidence, and together with the information of the sampling volume rate, the scattering data can be converted to size distributions of aspherical particles in the diameter range of 20–700  $\mu\text{m}$ . This information together with measurements from the 2DS was used to estimate ice particle concentrations below 100  $\mu\text{m}$ —also in mixed phase conditions (Fig. ES2).

After processing the data from the cloud probes separately, the data were combined to provide a best estimate of cloud microphysical properties that is not probe specific (E. Järvinen et al. 2021, unpublished manuscript; Wu et al. 2020), allowing those who are not familiar with the detailed operation of the probes to more readily use the data for process studies, parameterization development, and evaluation of model simulations and remote sensing retrievals. The probe-independent estimate for PSDs and total number concentrations ( $N_{\text{tot}}$ ) is provided for each phase (liquid and ice). The procedure of combining the different cloud probes is a subject of future publication but a brief description is given here. Additional information can be also found in E. Järvinen et al. (2020, unpublished manuscript), W. Wu et al. (2021, unpublished manuscript), and J. D'Alessandro et al. (2021, manuscript submitted to *J. Geophys. Res. Atmos.*). The probe-independent estimate for  $N_{\text{tot}}$  and PSDs was generated for different cloud hydrometeors types separately, 1) liquid particles, 2) ice particles, and 3) all particles combined depending on the cloud phase information based on the analysis of J. D'Alessandro et al. (2021, manuscript submitted to *J. Geophys. Res. Atmos.*). For supercooled liquid and warm clouds with only liquid particles, the  $N_{\text{tot}}$  ( $N_{\text{liquid}}$ ) and PSDs for all (liquid) particles was defined as a combination of CDP for particles with sizes  $1 < D_p < 50\text{ }\mu\text{m}$  and 2D-S for particle sizes  $50 < D_p < 1,600\text{ }\mu\text{m}$ . For ice clouds completely composed of ice particles, the  $N_{\text{tot}}$  ( $N_{\text{ice}}$ ) and PSDs for all (ice) particles was based on 2DS measurements for the size range

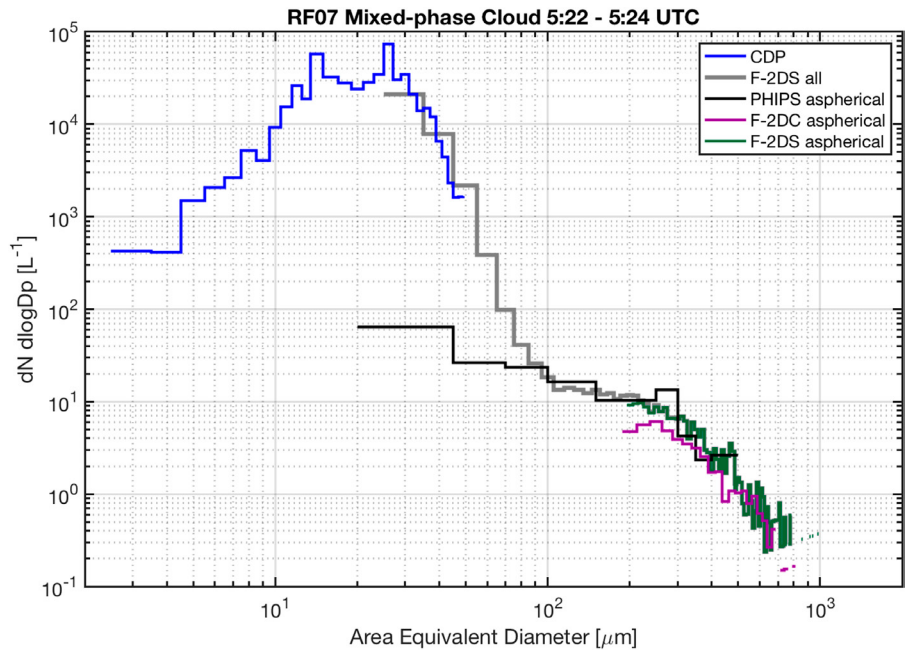


**Fig. ES2.** Size distributions of all particles from CDP (blue) and 2DS (gray), and of spherical particles with area equivalent diameter between 20 and 700  $\mu\text{m}$  from PHIPS, for 200–1,600  $\mu\text{m}$  from the 2DC, and for 200–1,900  $\mu\text{m}$  from the 2DS for a mixed-phase cloud measured between 0522 and 0524 UTC during RF07. The mean temperature during the sampling was  $-7^\circ\text{C}$ .

*Geophys. Res. Atmos.*). The probe-independent estimate for  $N_{\text{tot}}$  and PSDs was generated for different cloud hydrometeors types separately, 1) liquid particles, 2) ice particles, and 3) all particles combined depending on the cloud phase information based on the analysis of J. D'Alessandro et al. (2021, manuscript submitted to *J. Geophys. Res. Atmos.*). For supercooled liquid and warm clouds with only liquid particles, the  $N_{\text{tot}}$  ( $N_{\text{liquid}}$ ) and PSDs for all (liquid) particles was defined as a combination of CDP for particles with sizes  $1 < D_p < 50\text{ }\mu\text{m}$  and 2D-S for particle sizes  $50 < D_p < 1,600\text{ }\mu\text{m}$ . For ice clouds completely composed of ice particles, the  $N_{\text{tot}}$  ( $N_{\text{ice}}$ ) and PSDs for all (ice) particles was based on 2DS measurements for the size range

$10 < D_p < 1,600 \mu\text{m}$ . The 2DS was used for all flights, except for RF15, where 2DS data were not available and 2DC measurements were used instead.

To get ice particle concentrations in mixed-phase conditions, discrimination of the phase of individual cloud hydrometeors is needed. Reliable phase discrimination of 2DS data is possible only down to  $200 \mu\text{m}$  so PHIPS was used to get information on the ice phase of small ( $<200 \mu\text{m}$ ) cloud particles. The  $N_{\text{ice}}$  and PSDs for ice particles were defined as a combination of the PHIPS aspherical particles in the size range  $20 < D_p < 200 \mu\text{m}$  and 2DS aspherical particles in the size range  $200 < D_p < 1,600 \mu\text{m}$ . It should be noted that here  $D_p$  is defined as the volume equivalent diameter for both PHIPS and 2DS. The  $N_{\text{liquid}}$  and PSDs for liquid particles was defined as a combination of CDP measurements for the size range  $1 < D_p < 50 \mu\text{m}$  (assuming all particles were liquid), PHIPS spherical particles for the size range  $100 < D_p < 200 \mu\text{m}$  and 2DS spherical particles for the size range  $200 < D_p < 1,600 \mu\text{m}$ . The  $N_{\text{tot}}$  and PSDs for all particles was defined as a combination of CDP for particles with sizes  $1 < D_p < 50 \mu\text{m}$  and 2DS for particle sizes  $50 < D_p < 1,600 \mu\text{m}$ .

Figure ES3 outlines the basic flight strategy for SOCRATES. The southbound leg was conducted at approximately 7 km, collecting remote sensing data and releasing dropsondes to

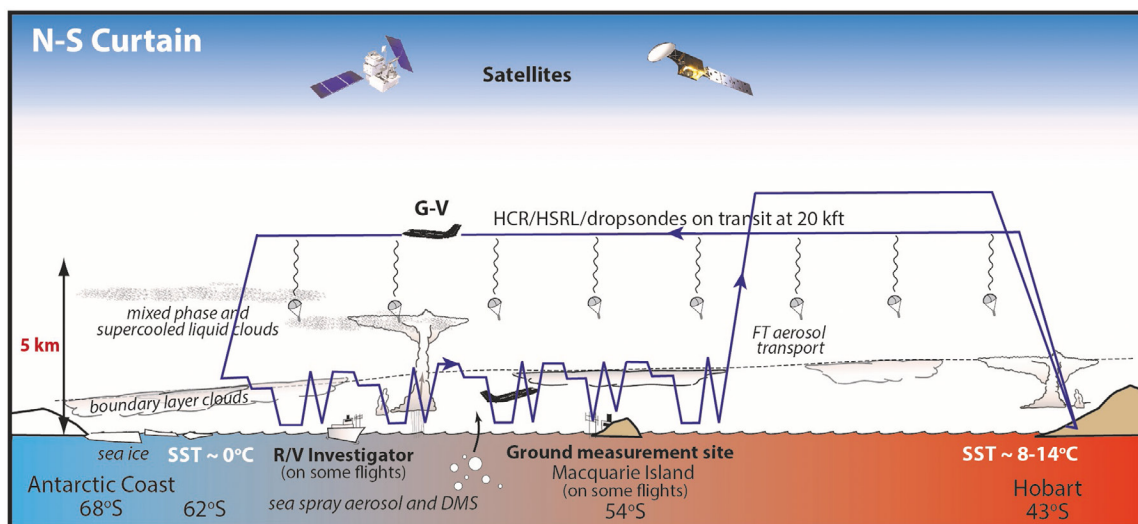


**Fig. ES3.** Flight sampling strategy employed for SOCRATES. NSF-NCAR G/V flew the southbound leg from Hobart in the free troposphere, mapping thermodynamic curtain with dropsondes while remotely probing clouds with HCR and HSRL as well as sampling free troposphere aerosols and occasionally clouds in situ. On the northbound leg returning toward Hobart, NSF-NCAR G-V flew clouds at constant altitude and using ramped ascents/descents, and measured aerosols above and below cloud in constant altitude legs. Overflights of Macquarie Island or R/V *Investigator* were executed on either low- or high-altitude legs whenever feasible.

obtain a north–south “curtain” of thermodynamic properties. The height of 7 km allowed sufficient sensitivity of the HCR to detect precipitation and some cloud, and allowed in situ sampling of some thin clouds with SLW at  $T < -30^\circ\text{C}$ . At its maximum range, typically around 62°S, the G-V descended to its lowest allowable altitude, nominally 150 m, and performed in situ sampling intermittently in the MBL and free troposphere while returning toward Hobart. This transect consisted of a series of low altitude legs below cloud to sample aerosol in the BL, a leg 300 m above cloud to sample free tropospheric aerosol, and combinations of level legs and ramped ascents/descents through clouds.

Table ES11 lists each of the SOCRATES missions, the objectives, conditions sampled and information on which probes malfunctioned on a flight. Any probe not listed is regarded to have performed well to the best of our current knowledge. The cloud and aerosol properties

**Table ES11. List of SOCrates missions, objectives, conditions sampled, and probes that malfunctioned or were unavailable on a flight. Any probe not listed is regarded to have performed well to the best of our current knowledge.**

IOP/date	Start time	End time	Objective	Summary/notes
RF01 15 Jan 2018	2254 UTC	0601 UTC + 1	Overcast stratocumulus in dry slot behind low at 60°S, 153°E	Multiple cloud levels in remote sensing leg; two levels of SLW for in situ sampling of weakly drizzling clouds; no downward-looking solar irradiance data available
RF02 19 Jan 2018	0051 UTC	0741 UTC	Supercooled cloud near 60°S, 140°E between two surface lows	Thin and sometimes patchy multilayered clouds between 2 and 6 km; in situ legs near surface, above and within cloud; no 2DC and RICE data available
RF03 22 Jan 2018	2102 UTC	0411 UTC + 1	Transition of clouds associated with low just west of Investigator	SLW near -30°C, generating cells near cloud top; RFP in free troposphere; persistent multilayer clouds with SLW; no gust probe data available
RF04 23 Jan 2018	2313 UTC	0612 UTC + 1	Transition of clouds associated with low near Investigator	Two aerosol sampling legs above cloud and above ocean surface; liquid water and drizzle noted above cloud top; two passes near Investigator
RF05 25 Jan 2018	2253 UTC	0555 UTC + 1	Coordinated sampling with Investigator	Sampled low cloud and aerosol in cold sector; frequent SLW noted at cloud top; low-level aerosol sampled prior to crossing cold front, and sawtooth profile through frontal band
RF06 28 Jan 2018	2254 UTC	0612 UTC + 1	Cold sector of midlatitude cyclone	Runs above, within, and below cloud as well as sawtooth in cold sector; multilayered low clouds and shallow cumuli sampled; some notable icing in first in-cloud run
RF07 31 Jan 2018	0058 UTC	0830 UTC	Cold air wrapped around low pressure and overflight of Macquarie Island	Extensive and persistent supercooled cloud; extensive sampling of icing layer in coordination with above/below aerosol; coordinated sondes at Macquarie Island; no gust probe data are available
RF08 3 Feb 2018	2315 UTC	0645 UTC + 1	Extensive area of low-level cloud associated with low pressure system	Three complete in situ modules (above/below/within cloud and sawtooths); some ice buildup on probes and large sea spray seen
RF09 4 Feb 2018	2255 UTC	0702 UTC + 1	Low-level cloud behind low pressure system and Macquarie Island overflight	Sampled cold sector in moderate icing with complete suite of above/within/below cloud legs and sawtooths, complete with sonde comparison over Macquarie Island
RF10 7 Feb 2018	2054 UTC	0511 UTC + 1	Standard curtain flight, but also sample frontal midlevel cloud out of Hobart	Diverse cloud and boundary layer types, including weak front crossing Tasmania and shallow nonprecipitating clouds
RF11 17 Feb 2018	0139 UTC	0622 UTC	Shallow cumulus clouds in cold air	No satellite communication; supercooled cumulus with 1 g m <sup>-3</sup> LWC and a few ice particles; no 2DS data are available for most of this flight
RF12 17 Feb 2018	2352 UTC	0753 UTC + 1	Extensive stratocumulus field around R/V <i>Investigator</i>	Liquid cloud tops with light snow precipitation, and stratocumulus/closed mesoscale cellular convective deck east of ridge near R/V <i>Investigator</i>
RF13 19 Feb 2018	2258 UTC	0636 UTC + 1	Large anticyclone SSE of Tasmania with shallow stratocumulus, including pass over Macquarie Island	Warm boundary layer stratocumulus, overflight of Macquarie Island, and standard sampling models on return; no 2DS data are available for most of this flight
RF14 21 Feb 2018	2248 UTC	0646 UTC + 1	Field of open cells and stratiform clouds further south	Very shallow clouds in northern part of leg, multilayer clouds with freezing layer near surface further south; icing noted in southern clouds, standard modules executed further north
RF15 24 Feb 2018	0206 UTC	0838 UTC	Field of cumulus in cold air with tops near -7°C	SLW up to 1 g m <sup>-3</sup> with few ice particles; some passes all liquid, whereas others mixed or all ice; updraft speeds up to 5 m s <sup>-1</sup> ; no 2DS data available

sampled during each flight, as well as those sampled by the ship and surface-based instrumentation, must be understood in the context of the meteorological setting at that time. On four flights, the G-V overflowed the R/V *Investigator*, yielding a more extensive dataset when combined with CAPRICORN II, and on two flights, the G-V overflowed Macquarie Island, providing additional data that could be analyzed jointly with the MICRE data. On two other flights,

the G-V deviated from its north–south transects to sample cumulus fields in the cold sector in the vicinity of 50°–55°S, and part of one flight was dedicated to sampling an atmospheric river just south of Tasmania.

A summary of the dates and INP sampling methods for the different campaigns are listed in Table ES12. Two INP measurements methods were used to cover  $0^{\circ}\text{C} < T < -30^{\circ}\text{C}$ . Two identical Colorado State University (CSU) CFDC (DeMott et al. 2017) were deployed on the G-V and in both CAPRICORN voyages. The instruments were operated well above water saturation to

**Table ES12.** Ice nucleating particle measurements in SOAR-related studies, including measurement periods, measurement methods, and locations. Studies conducted prior to the 2017–18 period are included. SOCRATES here refers only to measurements at altitude on the G-V, CAPRICORN to measurements on the R/V *Investigator*, MARCUS to measurements on the RSV *Aurora Australis*, and TAN to measurements on the R/V *Tangaroa*. MICRE was the only fixed site, at Macquarie Island.

Study	Platform	Dates	Method	Lat or max. range (frac. °)	Lon or max. range (frac. °)
SOCRATES	NSF–NCAR G-V	15 Jan–27 Feb 2018	CFDC, IS	-46.2 to -61.3	135.4 to 161.5
MICRE	Macquarie Island Station	15 Mar 2017–15 Mar 2018	IS	-54.5	158.95
MARCUS	RSV Aurora Australis	2 Nov 2017–26 Mar 2018	IS	-43.5 to -68.6	62.8 to 158.9
CAPRICORN II	R/V Investigator	11 Jan–23 Feb 2018	CFDC, IS	-42.8 to -66.5	132 to 150
CAPRICORN I	R/V Investigator	18 Mar–14 Apr 2016	CFDC, IS	-44.4 to -51.6	142.3 to 149.8
TAN1502 <sup>a</sup>	R/V Tangaroa	28 Jan–10 Mar 2015	IS	-41.7 to -74.7	162.1 to -174.9

<sup>a</sup> TAN1502 (Welti et al. 2020) refers to the New Zealand–Australia Antarctic Marine Ecosystems voyage of the NIWA R/V Tangaroa vessel, which occurred from 28 Jan to 10 Mar 2015 (UTC), sailing from Wellington, New Zealand, to the Ross Sea and back. The voyage included underway oceanographic and atmospheric observations.

emphasize immersion freezing activation (DeMott et al. 2017) on single INPs up to sizes of about  $2\text{ }\mu\text{m}$ , as limited by upstream inertial impactors required for differentiating nucleating ice crystals from aerosol. Due to the low sample flow rate ( $1.5\text{ }(\text{volumetric L min}^{-1})$ ), low INP number concentrations encountered, and limited times that could be spent by the G-V in a single atmospheric layer ( $\sim 10\text{ min}$ ), CFDC measurements were typically made at  $T < -25^{\circ}\text{C}$ . Clear air INPs (above clouds and in the MBL) were sampled using a HIAPER modular inlet (HIMIL) (Stith et al. 2009) on the G-V belly. CFDC data were also collected on dried (using diffusion driers) cloud residual particles from the CVI inlet during descents, ascents, and sawtooth patterns through clouds.

The CSU ice spectrometer (IS) was used to measure immersion freezing temperature spectra on bulk aerosol samples (no upper size limit) collected onto polycarbonate membrane filters (typical pore size of  $0.2\text{ }\mu\text{m}$ ) (e.g., McCluskey et al. 2018) in open-faced samplers filtering air for long periods in the ship campaigns (CAPRICORN I, CAPRICORN II, and MARCUS) and during MICRE, and within inline metal holders mounted in the CFDC rack to also sample from the HIMIL (located on the G-V belly) on the G-V. No size selectivity is assumed for the ship or MICRE filter collections, while limited transfer of particles larger than  $3\text{ }\mu\text{m}$  is expected based on loss calculations for the inline filters on the G-V. IS measurements covered ice nucleation from the highest  $T$  that detection limits would allow to  $-27^{\circ}\text{C}$ . The IS detection limit, or the lowest INP concentration that could be measured and consequently the highest  $T$  at which INP concentration could be assessed, varied depending upon the sample volume collected on each filter. Filter collection times were most limited on the G-V, and flow rates per standard liter (sL) decreased with altitude, resulting in collected volumes of 50–600 sL. Filters on the ships and during MICRE were collected from 24 to 72 h, accumulating volumes of 10,000 to 70,000 sL. Separate INP filter samples representative of above and below cloud regions were collected intermittently on the G-V and integrated over a range of geographic positions to obtain sufficient sample volume. Select numbers of filters in each campaign were processed

for immersion freezing studies of aerosol suspensions following thermal and chemical treatments to discern the contributions of biological, organic, and inorganic INPs (McCluskey et al. 2018). These INP data, and additional selected aerosol chemical ionic, total organic carbon, and total organic nitrogen analyses of filter-collected aerosols are the subject of continuing analyses and archival product developments.

### Supplementary results

The remote sensing and in situ samplers were used in synergy so that the necessary detail on cloud and vertical characteristics over the BL and free troposphere could be used for constraining and evaluating models. For example, Fig. ES4 shows an analysis of in situ data and collocated particle-type retrieval based on the G-V W-band cloud radar and HSRL using a fuzzy-logic algorithm (Vivekanandan et al. 1999). In this example the temperature ranges from  $-8.5^{\circ}\text{C}$  at cloud base to  $-10.5^{\circ}\text{C}$ . In the lower part of clouds, supercooled drizzle (corresponding to  $D > 75 \mu\text{m}$ ) measured by a 2DC was comingled with cloud droplets ( $D < 50 \mu\text{m}$ ) measured by a CDP, whereas in the upper 100 m of the clouds only small particles were detected. The HSRL backscatter and depolarization ratio are included in Fig. ES4 to show how these variables responded to the observed mix of small and large drops (drizzle). Overall, the particle typing technique identifies the stronger drizzle regions, and the presence of supercooled cloud droplets near cloud top, consistent with the in situ data.

Radar reflectivity from the BASTA W-band cloud radar, the 31-GHz brightness temperature from the two-channel microwave radiometer and 355-nm attenuated backscatter from the RMAN lidar system together provide significant constraints on cloud microphysical properties. This is particularly true when the clouds reside in the MBL, are not precipitating, and are composed entirely of liquid phase cloud droplets. The radar reflectivity distributions in Figs. ES1d–f from layers fully contained in the MBL show that such nonprecipitating conditions (dBZ less than or equal to approximately  $-20$ ) were common at all latitudes during CAPRICORN II. That these layers were liquid phase and nonprecipitating make deriving their microphysical properties from remote sensing data reasonably straightforward. The algorithm introduced in Mace and Protat (2018b) has been adapted to derive the cloud microphysics using an optimal estimation methodology. The approach is fully described in Mace et al. (2020) where the algorithm is applied to data from CAPRICORN I, II, and MARCUS.

In situ cloud properties observed during SOCRATES are being used to evaluate cloud microphysical property retrievals based on the bispectral (Nakajima and King 1990) technique, frequently used in conjunction with *Himawari-8* and other imagers, including the operational Moderate Resolution Imaging Spectroradiometer (MODIS) level 2 (collection 6.1) cloud optical properties product and the CERES-MODIS (edition 4) cloud products. The results of this analysis will be reported in a separate article (Kang et al. 2021). Overall the bispectral retrievals compare well with the in situ data for SO stratocumulus, but with some bias in the retrieved effective radius and with some difficulties retrieving  $N_c$  when multiple thin low-altitude cloud layers are present. The satellite retrieved effective radius is slightly biased high (by about  $0.5\text{--}1.0 \mu\text{m}$ ) for non- and lightly drizzling cases and biased low by a large amount (about  $3\text{--}4 \mu\text{m}$ ) in some heavily drizzling cases.

Comparison against remote sensing measurements during the field projects has also been made. Cape Grim lidar (Alexander and Protat 2018) and CAPRICORN cloud radar–lidar observations (Mace and Protat 2018a,b; Protat et al. 2017) provided first insights into the morphology, frequency, vertical distribution, water content, and phase of SO clouds to complement existing satellite statistics as well as enabling evaluation of *Himawari-8* cloud products (Huang et al. 2019). CAPRICORN observations have also informed the development and contributed to the evaluation of new and very promising SLW mixed-phase cloud detection algorithms for geostationary satellites (Noh et al. 2019). First studies using CAPRICORN data have shown

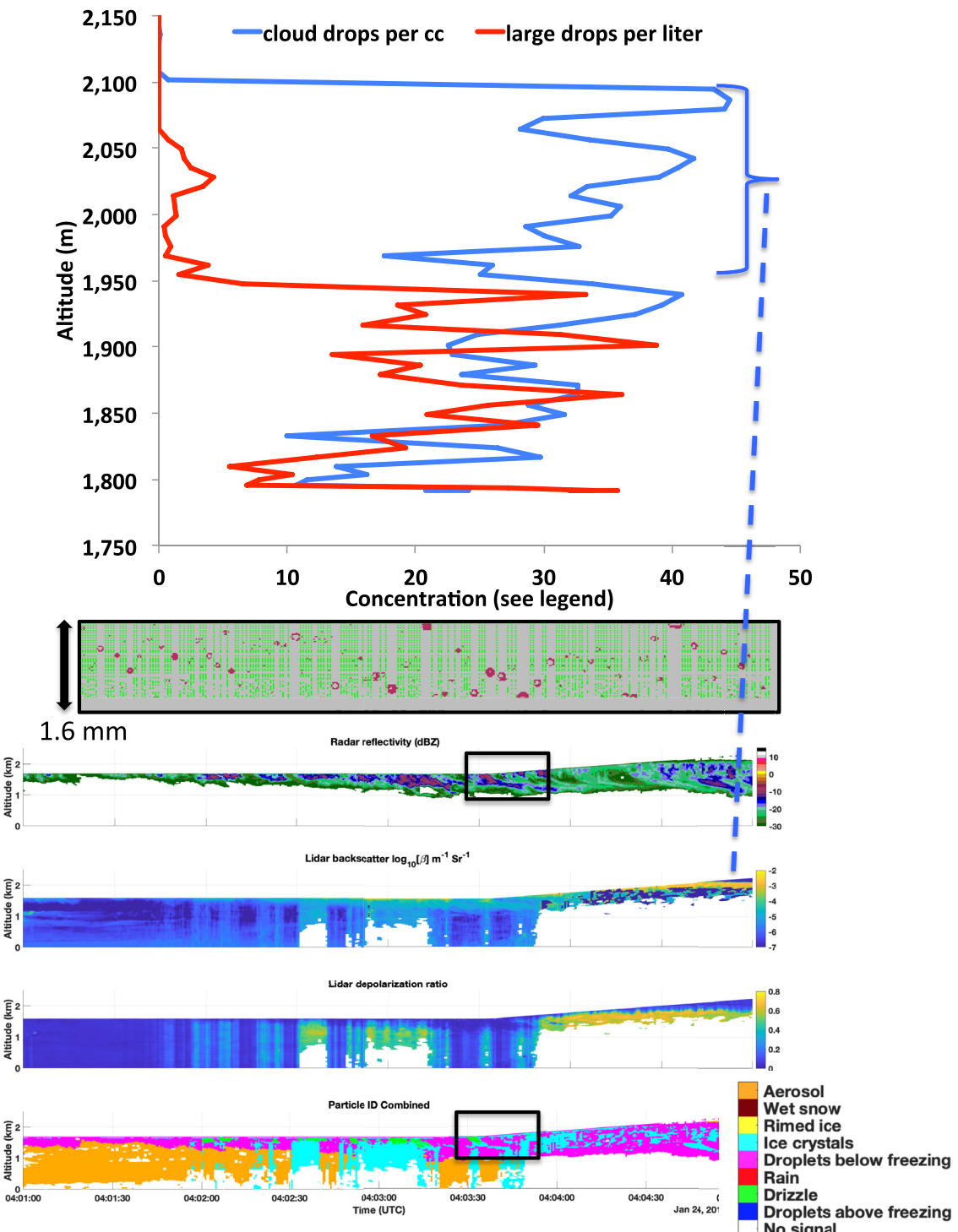


**Fig. ES4.** A comparison of the in situ and remote sensing measurements during an encounter with drizzle on 24 Jan 2018. Black boxes indicate drizzle imagery from the optical array probe and corresponding radar reflectivity and particle ID. The dashed line indicates where the top 100-m layer of cloud drops was detected by the lidar during the climb in the latter part of the pass. See text for more explanation.

that statistical estimates of cloud phase from ground-based and satellite are disparate (e.g., Alexander and Protat 2018; Mace and Protat 2018b), owing to different geometries of observations resulting in a different and problematic conditional sampling of cloud population. Observations of cloud systems close to the Antarctic coast made during MARCUS indicate the common occurrence of multiple SLW layers, along with evidence of seeding of single-layer SLW

by higher-altitude ice clouds present near the end of the life of cyclones (Alexander et al. 2020, manuscript submitted to *J. Geophys. Res. Atmos.*).

Hygroscopic growth factor (HGF) distributions at 90% RH averaged for CAPRICORN I are shown in Fig. ES5. HGF measurements indicate size-dependent particle composition between the Aitken and accumulation modes, with the Aitken mode made up almost entirely of particles with HGFs

similar to those for non-sea salt sulfates. Accumulation mode HGFs have a larger component made up of high hygroscopicity sea salt. Further, the number fraction of high hygroscopicity sea salt is lower than the sea spray number fraction estimated from volatility, indicating that the accumulation of sulfate and depletion of chlorine during aging and cloud processing is likely to reduce the particle hygroscopicity. As shown in the “BL aerosol and CCN vary according to origin” section in the main paper, chemical analysis of the marine boundary layer aerosol during SOCRATES indicated that aged or processed sea spray makes up an important contribution to the total sea spray number.

The chemical functionality of the organic compounds present in particles sampled by the CVI in the BL was characterized by STXM-NEXAFS at the Advanced Light Source of Lawrence Berkeley Laboratory (Saliba et al. 2021) for 96 particles, as shown in Fig. ES6. Measured particles included geometric diameters from 0.2 to 2  $\mu\text{m}$ , with approximately half with sizes of 0.7  $\mu\text{m}$  or larger. Many of the particles sampled in this size range had low or no detectable amounts of carbonaceous components. For the particles with carbon absorption above detection, the NEXAFS spectra showed a variety of mixtures of organic functional

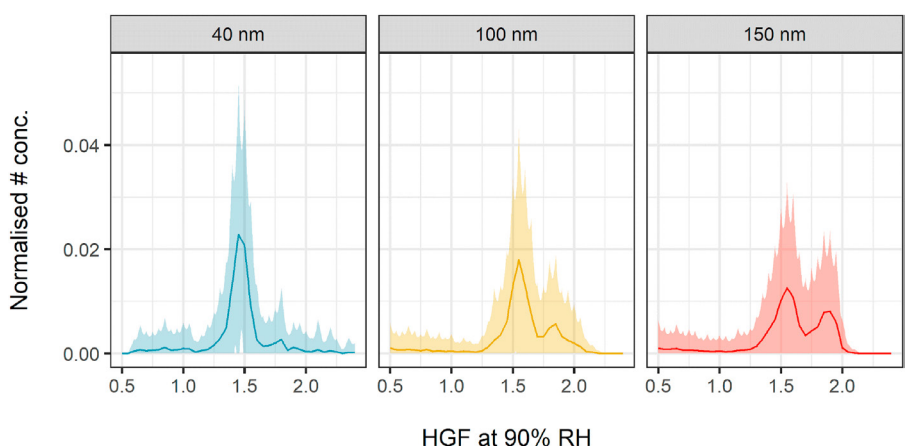


**Fig. ES5.** Mean hygroscopic growth factor distributions measured using the H-TDMA during the CAPRICORN I. Preselected particle diameters were 40 nm (blue), 100 nm (yellow), and 150 nm (red). Shading represents the standard deviation mean for each HGF bin at each preselected particle size.

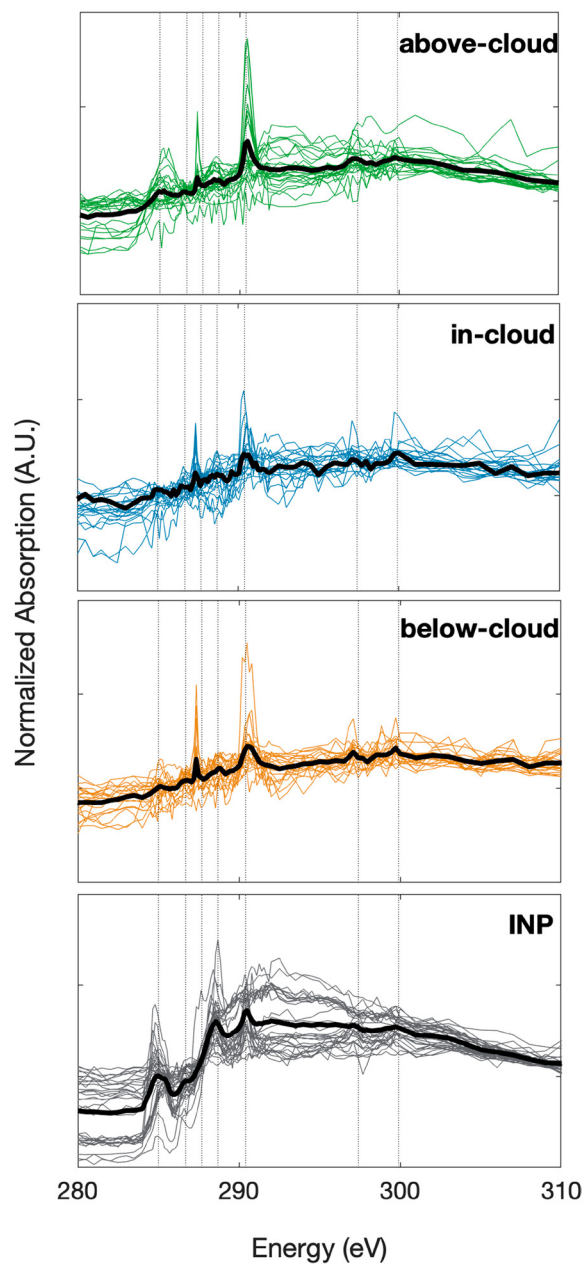


**Fig. ES6.** Normalized absorption vs beam energy for the 96 particles analyzed with STXM-NEXAFS. The spectra are grouped by below-cloud, in-cloud, above-cloud, and INP categories. Vertical dotted lines correspond to R(C=C)R' (285.0 eV), R(C=O)R (286.7 eV), R(CH<sub>n</sub>)R' (287.7 eV), R(C=O)OH (288.7 eV), CO<sub>3</sub><sup>2-</sup> (290.4 eV), and potassium (297.4 and 299.9 eV) transitions.

groups similar to classes identified previously in marine and continental sampling (Hawkins and Russell 2010; Takahama et al. 2007). A number of particles had composition previously attributed to marine sources with functional groups consistent with polysaccharides, some of which also contained evidence of crystallized NaCl (Saliba et al. 2021). Figure ES6 shows a comparison of particles collected below cloud, in cloud, and above cloud showed small average differences, except that the above cloud particles had more carbonate absorption than the below and in cloud samples. The similarity of the composition between below cloud and in cloud samples is consistent with there being few organic functional group differences between the particles that activate and those that do not, consistent with organic components being a small mass fraction of activated CCN. The general similarity of the above, in and below clouds indicates that mixing between these levels is recent. The high carbonate could indicate long-range transported dust particles. The INPs sampled showed the most distinct signature of carboxylic acid group absorbance, as well as a clear aromatic or unsaturated carbon signature.

The back trajectories were combined with the ECMWF reanalysis cloud fraction 6-h data to identify relationships between boundary layer cloud fraction and particle concentrations. Over a 24-h back trajectory, the boundary layer cloud fraction ranged from 0.22 to 1.0 with an average of  $0.64 \pm 0.24$  ( $1 - \sigma$ ). The highest CN concentrations almost exclusively correspond to lower occurrences of boundary layer clouds, with an average cloud fraction of  $0.47 \pm 0.19$ , and most likely result from recent particle formation (RPF). This is consistent with previous findings on RPF events occurring under low cloud cover or high solar radiation due to enhanced photooxidation of DMS (O'Dowd et al. 1998; Kerminen et al. 2018). The cluster with low CN/low CCN consisted of westerly and southerly back trajectories, which consistently had precipitation within the previous 48 h upstream. The ECMWF reanalysis (Dee et al. 2011) total precipitation amount, averaged over the 48-h back trajectory, inversely correlated with CCN number concentrations at 0.3% supersaturation ( $r = 0.49$ ). Both clusters with low CCN concentrations had been impacted by precipitation within 48 h prior to sampling.

An unanticipated opportunity to measure the structure and microphysics of an atmospheric river (AR) over Tasmania and the SO with the G-V occurred on 29 January 2018. The AR originated near the northwest Australian coast within the monsoon trough associated with the ITCZ, and flowed southeastward across Australia, Tasmania, and the SO to a latitude of  $60^{\circ}$ S (Fig. ES7). During departure from Hobart, the G-V ascended and passed through the AR, and later upon return to Hobart, dropped sondes across the AR, then descended from 7-km altitude to near the surface within the AR. G-V dropsonde, radar, and microphysical measurements, *Himawari-8* satellite cloud-top temperature and altitude retrievals, and GPM radar analyses were used in conjunction with WRF simulations with water vapor tracers to investigate the relative contributions

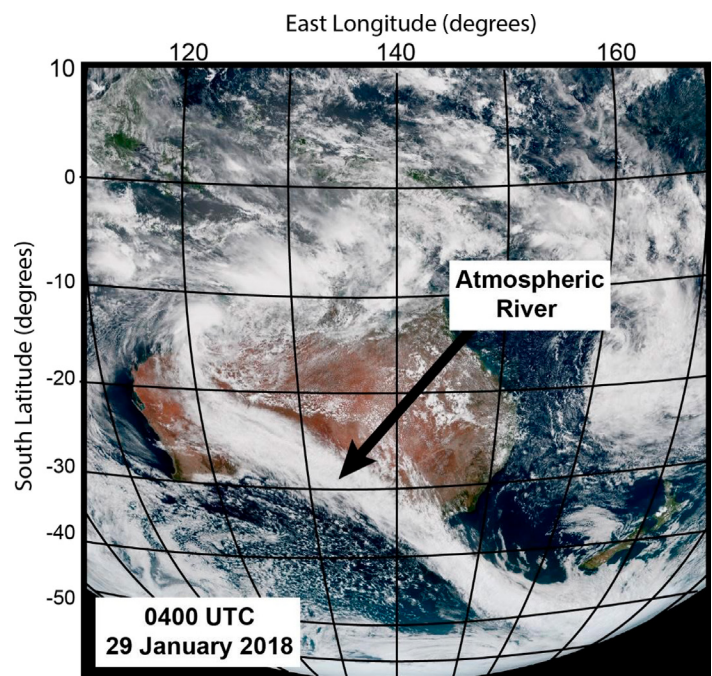


**Fig. ES7.** Visible satellite image of the Southern Hemisphere from the *Himawari-8* satellite showing the cloud field associated with the atmospheric river and tropical convection along the intertropical convergence zone (ITCZ) at 0400 UTC 29 Jan 2018.

of tropical and midlatitude moisture sources to the AR as well as microphysical processes occurring within the rainbands composing the AR. Analyses show that moisture associated with a monsoonal tropical depression became entrained into the AR along a strong midlatitude frontal system that extended to 60°S over the SO. Moisture from the monsoon trough precipitated all the way to the high latitudes, demonstrating that ARs provide a direct connection between the tropics and polar regions (Rauber et al. 2020; Finlon et al. 2020).

**Additional details on modeling efforts.** As previously mentioned, modeling was an integral component of the SO projects. Table ES13 lists the different models that have been simulating SO clouds as part of the multiagency consortium, as well as the approximate grid resolution and purpose of their modeling work.

**Table ES13. Different models used to simulate SO conditions, approximate grid resolution and purpose of modeling work.**

Institution	Model	Type	Resolution	PI
NCAR	CAM6	GCM	~100 km	Gettelman, Bardeen
GFDL	AM4	GCM	~100 km	Lin, Ming
UWash	LES	SAM6.11	50 m	Atlas, Blossey
BoM	ACCESS-R	Regional forecast	12 km	Protat
BoM	ACCESS-C	"City-scale" forecast	4 km	Protat
Monash	WRF	Mesoscale	27/9/3 km	Huang, Siems
Stony Brook	GlobalSAM	GCRM	2 km	Khairoutdinov, Atlas
U. Ill	CM1/WRF	CRM/mesoscale	50 m	Lasher-Trapp/Jewett
U. Stockholm	NorESM	GCM	200 km	Frey

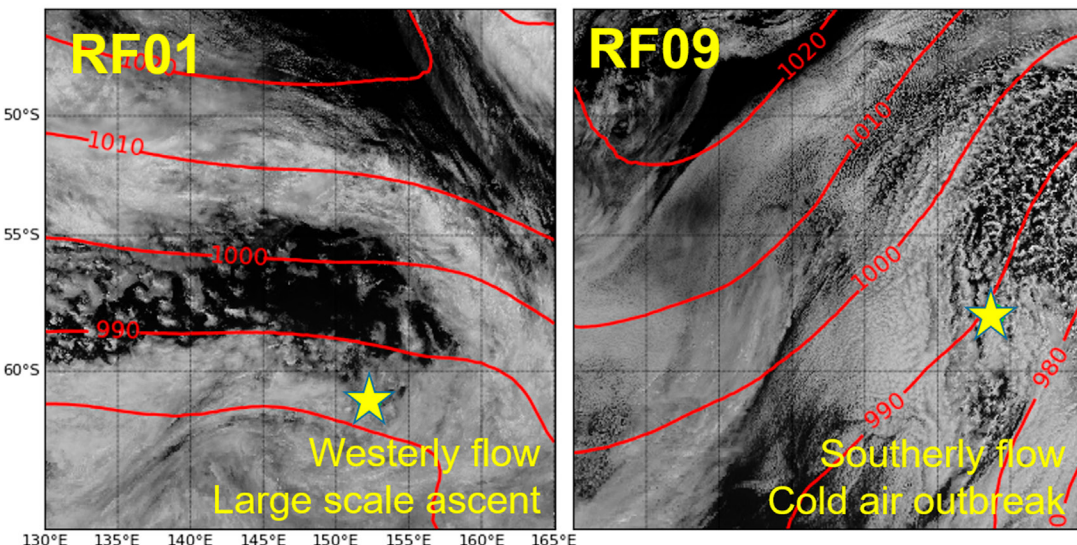
Models with grids fine enough to resolve turbulent eddies and sharp temperature inversions are required to simulate the tight interaction between clouds and turbulence within SO cloudy boundary layers. Atlas et al. (2020) simulated six SOCRATES cases using the System for Atmospheric Modeling (SAM) LES (Khairotudinov and Randall 2003) with 50-m horizontal and 10-m vertical grid resolution and compared the SAM results with nudged CAM6 and AM4. Figure ES8 depicts simulations of a two-layer stratus case (RF01) and a case of cumulus rising into stratocumulus (RF09), demonstrating that SAM is able to broadly capture the structure of the cloud fields in both regimes.

SOCRATES clouds are dominated by supercooled water and feature highly variable concentrations of cloud droplets and large frozen particles, which are challenging to simulate. SAM LES consistently simulates supercooled clouds whereas CAM6 and AM4 skillfully maintain supercooled water within stratiform clouds but tend to excessively glaciate cumulus clouds. The Morrison et al. (2005) microphysics scheme in the LES underestimates the secondary production of ice in clouds occupying the Hallett–Mossop temperature range (from  $-3^{\circ}$  to  $-8^{\circ}\text{C}$ ). This bias is improved by removing arbitrary thresholds in the parameterization that inactivate the Hallett–Mossop process in SOCRATES clouds.

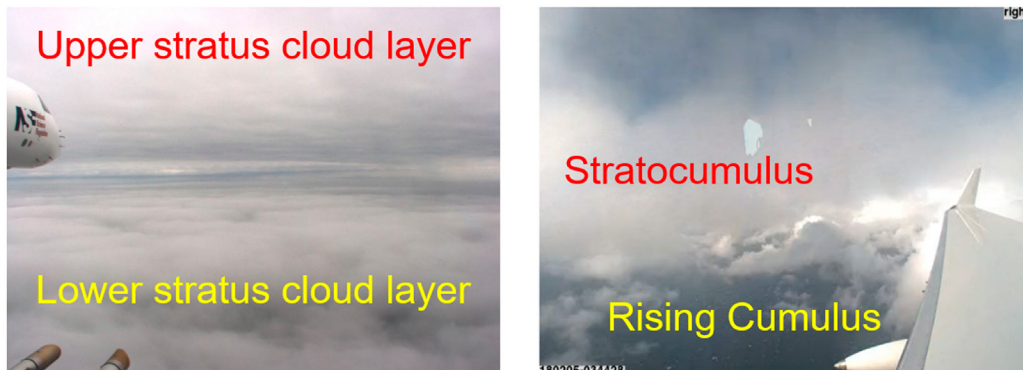
The LES uses observationally specified fixed droplet concentrations, whereas CAM6 and AM4 prognose an aerosol concentration that is used to activate droplets. CAM6 underestimates droplet concentrations by 25%–100%, whereas AM4, despite simpler one-moment microphysics and aerosol treatments, has less bias. Atlas et al. (2020) suggest that deficiencies in turbulent vertical updraft velocity and premature glaciation contribute to low droplet concentrations in CAM6.

# Example LES cases

Visible reflectance from Himawari with sea level pressure contours from ERA5



Representative Images from the G/V Aircraft



Simulated clouds from the LES

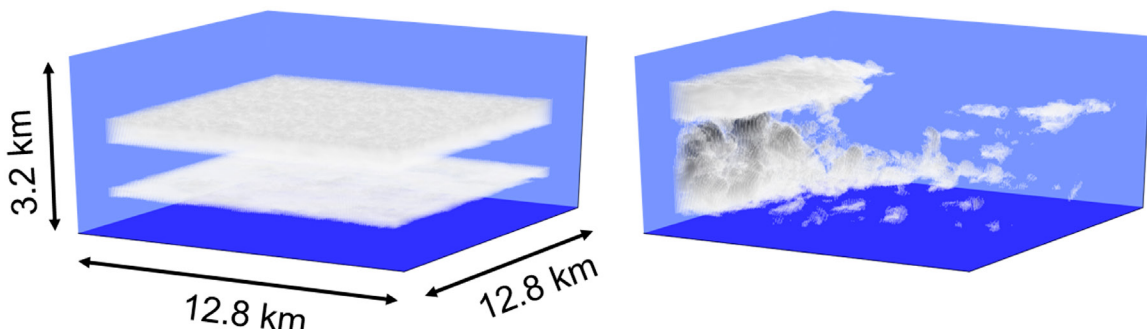


Fig. ES8. (top) Satellite observations, (middle) in situ aircraft images, and (bottom) LES simulated clouds are shown for two SOCRATES cases. (left) RF01 features two decoupled stratus layers in a stable boundary layer. (right) RF09 features cumulus rising into stratocumulus in an unstable boundary layer. Yellow stars in the top row indicate locations of the in situ aircraft measurements.

## References

- Abdelmonem, A., E. Järvinen, D. Duft, E. Hirst, S. Vogt, T. Leisner, and M. Schnaiter, 2016: PHIPS-HALO: The airborne particle habit imaging and polar scattering probe—Part I: Design and operation. *Atmos. Meas. Tech.*, **9**, 3131–3144, <https://doi.org/10.5194/amt-9-3131-2016>.
- Alexander, S. P., and A. Protat, 2018: Cloud properties observed from the surface and by satellite at the northern edge of the Southern Ocean. *J. Geophys. Res. Atmos.*, **123**, <https://doi.org/10.1002/2017JD026552>.
- Armour, K. C., J. Marshall, J. R. Scott, A. Donohoe, and E. R. Newsom, 2016: Southern Ocean warming delayed by circumpolar upwelling and equatorward transport. *Nat. Geosci.*, **9**, 549–554, <https://doi.org/10.1038/ngeo2731>.
- Atlas, R. L., C. S. Bretherton, and P. N. Blossey, 2020: How well do high and low resolution models represent observed boundary layer structures and low clouds over the summertime Southern Ocean? *J. Geophys. Res.*, **125**, e2020MS002205, <https://doi.org/10.1029/2020MS002205>.
- Baumgardner, D., and Coauthors, 2017: Cloud ice properties: In-situ measurement challenges. *Ice Formation and Evolution in Clouds and Precipitation: Measurement and Modeling Challenges*, Meteor. Monogr., No. 58, Amer. Meteor. Soc., <https://doi.org/10.1175/AMSMONOGRAPHSD-16-0011.1>.
- Bharti, V., E. Schulz, C. W. Fairall, B. W. Blomquist, Y. Huang, A. Protat, S. T. Siems, and M. J. Manton, 2019: Assessing surface heat flux products with in-situ observations over the Australian sector of the Southern Ocean. *J. Atmos. Oceanic Technol.*, **36**, 1849–1861, <https://doi.org/10.1175/JTECH-D-19-0009.1>.
- Cadeddu, M. P., J. C. Liljegren, and D. D. Turner, 2013: The Atmospheric Radiation Measurement (ARM) program network of microwave radiometers: Instruments, data, and retrievals. *Atmos. Meas. Tech.*, **6**, 2359–2372, <https://doi.org/10.5194/amt-6-2359-2013>.
- Dee, D. P., and Coauthors, 2011: The ERA-Interim reanalysis: Configuration and performance of the data assimilation system. *Quart. J. Roy. Meteor. Soc.*, **137**, 553–597, <https://doi.org/10.1002/qj.828>.
- Delanoë, J., and Coauthors, 2016: BASTA, a 95 GHz FMCW Doppler radar for cloud and fog studies. *J. Atmos. Oceanic Technol.*, **33**, 1023–1038, <https://doi.org/10.1175/JTECH-D-15-0104.1>.
- DeMott, P. J., and Coauthors, 2017: Comparative measurements of ambient atmospheric concentrations of ice nucleating particles using multiple immersion freezing methods and a continuous flow diffusion chamber. *Atmos. Chem. Phys.*, **17**, 11227–11245, <https://doi.org/10.5194/acp-17-11227-2017>.
- , and Coauthors, 2018: The Fifth International Workshop on Ice Nucleation phase 2 (FIN-02): Laboratory intercomparison of ice nucleation measurements. *Atmos. Meas. Tech.*, **11**, 6231–6257, <https://doi.org/10.5194/amt-11-6231-2018>.
- Eloranta, E. W., 2005: High Spectral Resolution Lidar. *Lidar: Range-Resolved Optical Remote Sensing of the Atmosphere*, K. Weitkamp, Ed., Springer Series in Optical Sciences, Vol. 102, Springer-Verlag, 143–164.
- Finlon, J. A., and Coauthors, 2020: Structure of an atmospheric river over Australia and the Southern Ocean. II: Microphysical evolution. *J. Geophys. Res. Atmos.*, **125**, e2020JD032514, <https://doi.org/10.1029/2020JD032514>.
- Hawkins, L. N., and L. Russell, 2010: Polysaccharides, proteins, and phytoplankton fragments: Four chemically distinct types of marine primary organic aerosol classified by single particle spectromicroscopy. *Adv. Meteor.*, **2010**, 612132, <https://doi.org/10.1155/2010/612132>.
- Huang, Y., C. N. Franklin, S. T. Siems, M. J. Manton, T. Chubb, A. Lock, S. Alexander, and A. Klekociuk, 2015: Evaluation of boundary-layer cloud forecasts over the Southern Ocean in a limited-area numerical weather prediction system using in situ, space-borne and ground-based observations. *Quart. J. Roy. Meteor. Soc.*, **141**, 2259–2276, <https://doi.org/10.1002/qj.2519>.
- , S. Siems, M. Manton, A. Protat, L. Majewski, and H. Nguyen, 2019: Evaluating *Himawari-8* cloud products using shipborne and *CALIPSO* observations: Cloud-top height and cloud-top temperature. *J. Atmos. Oceanic Technol.*, **36**, 2327–2347, <https://doi.org/10.1175/JTECH-D-18-0231.1>.
- Johnson, G., Z. Ristovski, and L. Morawska, 2004: Method for measuring the hygroscopic behaviour of lower volatility fractions in an internally mixed aerosol. *J. Aerosol Sci.*, **35**, 443–455, <https://doi.org/10.1016/j.jaerosci.2003.10.008>.
- , C. Fletcher, N. Meyer, R. Modini, and Z. Ristovski, 2008: A robust, portable H-TDMA for field use. *J. Aerosol Sci.*, **39**, 850–861, <https://doi.org/10.1016/j.jaerosci.2008.05.005>.
- Kang, L., R. T. Marchand, and W. Smith, 2021: Evaluation of MODIS and *Himawari-8* low clouds retrievals over the Southern Ocean with in situ measurements from the SOCRATES campaign. *Earth Space Sci.*, **8**, e2020EA001397, <https://doi.org/10.1029/2020EA001397>.
- Kerminen, V. M., X. Chen, V. Vakkari, T. Petäjä, M. Kulmala, and F. Bianchi, 2018: Atmospheric new particle formation and growth: Review of field observations. *Environ. Res. Lett.*, **13**, 103003, <https://doi.org/10.1088/1748-9326/AAdf3c>.
- Khairoutdinov, M. F., and D. Randall, 2003: Cloud resolving modeling of the ARM summer 1997 IOP: Model formulation, results, uncertainties and sensitivities. *J. Atmos. Sci.*, **60**, 607–625, [https://doi.org/10.1175/1520-0469\(2003\)060<0607:CRMOTA>2.0.CO;2](https://doi.org/10.1175/1520-0469(2003)060<0607:CRMOTA>2.0.CO;2).
- Klekociuk, A. R., W. J. R. French, S. P. Alexander, P. Kuma, and A. J. McDonald, 2020a: The state of the atmosphere in the 2016 southern Kerguelen Axis campaign region. *Deep-Sea Res. II*, **174**, <https://doi.org/10.1016/j.dsr2.2019.02.001>.
- , D. J. Ottaway, A. D. MacKinnon, I. M. Reid, L. V. Twigger, and S. P. Alexander, 2020b: Australian lidar measurements of aerosol layers associated with the 2015 Calbuco eruption. *Atmosphere*, **11**, 124, <https://doi.org/10.3390/atmos11020124>.
- Lawson, R. P., D. O'Connor, P. Zmarzly, K. Weaver, B. Baker, Q. Mo, and H. Jonsson, 2006: The 2D-S (stereo) probe: Design and preliminary tests of a new airborne, high-speed, high-resolution particle imaging probe. *J. Atmos. Oceanic Technol.*, **23**, 1462–1477, <https://doi.org/10.1175/JTECH1927.1>.
- Mace, G. G., and A. Protat, 2018a: Clouds over the Southern Ocean as observed from the R/V *Investigator* during CAPRICORN. Part I: Cloud occurrence and phase partitioning. *J. Appl. Meteor. Climatol.*, **57**, 1783–1803, <https://doi.org/10.1175/JAMC-D-17-0194.1>.
- , and —, 2018b: Clouds over the Southern Ocean as observed from the R/V *Investigator* during CAPRICORN. Part II: The properties of nonprecipitating stratocumulus. *J. Appl. Meteor. Climatol.*, **57**, 1805–1823, <https://doi.org/10.1175/JAMC-D-17-0195.1>.
- , S. Benson, and Y. Hu, 2020: On the frequency of occurrence of the ice phase in supercooled Southern Ocean low clouds derived from CALIPSO and CloudSat. *Geophys. Res. Lett.*, **47**, e2020GL087554, <https://doi.org/10.1029/2020GL087554>.
- Marchand, R., T. Ackerman, E. R. Westwater, S. A. Clough, K. Cady-Pereira, and J. C. Liljegren, 2003: An assessment of microwave absorption models and retrievals of cloud liquid water using clear-sky data. *J. Geophys. Res.*, **108**, 4773, <https://doi.org/10.1029/2003JD003843>.
- McCluskey, C. S., T. C. J. Hill, R. S. Humphries, and A. M. Rauker, 2018: Observations of ice nucleating particles over Southern Ocean waters. *Geophys. Res. Lett.*, **45**, 11 989–11 997, <https://doi.org/10.1029/2018GL079981>.
- McFarquhar, G. M., and Coauthors, 2017: Processing of ice cloud in situ data collected by bulk water, scattering, and imaging probes: Fundamentals, uncertainties, and efforts toward consistency. *Ice Formation and Evolution in Clouds and Precipitation: Measurement and Modeling Challenges*, Meteor. Monogr., No. 58, Amer. Meteor. Soc., <https://doi.org/10.1175/AMSMONOGRAPHSD-16-0007.1>.
- Morrison, H., J. A. Curry, and V. I. Khvorostyanov, 2005: A new double moment microphysics scheme for application in cloud and climate models. Part I: Description. *J. Atmos. Sci.*, **62**, 1665–1677, <https://doi.org/10.1175/JAS3446.1>.
- Münkel, C., N. EresmAA, J. Rasainen, and A. Karppinen, 2007: Retrieval of mixing height and dust concentration with lidar ceilometer. *Bound.-Layer Meteor.*, **124**, 117–128, <https://doi.org/10.1007/s10546-006-9103-3>.
- Nakajima, T., and M.D. King, 1990: Determination of the optical thickness and effective particle radius of clouds from reflected solar radiation measurements. Part I: Theory. *J. Atmos. Sci.*, **47**, 1878–1893, [https://doi.org/10.1175/1520-0469\(1990\)047<1878:DOTOTA>2.0.CO;2](https://doi.org/10.1175/1520-0469(1990)047<1878:DOTOTA>2.0.CO;2).
- Noh, Y.-J., S. D. Miller, A. K. Heidinger, G. Mace, A. Protat, and S. P. Alexander, 2019: Satellite-based detection of daytime supercooled liquid-topped mixed-phase

- clouds over the Southern Ocean using the Advanced Himawari Imager. *J. Geophys. Res. Atmos.*, **124**, 2677–2701, <https://doi.org/10.1029/2018JD029524>.
- O'Dowd, C. D., M. Geever, M. K. Hill, M. H. Smith, and S. G. Jennings, 1998: New particle formation: Nucleation rates and spatial scales in the clean marine coastal environment. *Geophys. Res. Lett.*, **25**, 1661–1664, <https://doi.org/10.1029/98GL01005>.
- Protat, A., E. Schulz, L. Rikus, Z. Sun, and Y. Xiao, 2017: Shipborne observations of the radiative effect of Southern Ocean clouds. *J. Geophys. Res. Atmos.*, **122**, 318–328, <https://doi.org/10.1002/2016JD026061>.
- Rauber, R. M., H. Hu, F. Dominguez, S. W. Nesbitt, G. M. McFarquhar, T. Zaremba, and J. Finlon, 2020: Structure of an atmospheric river over Australia and the Southern Ocean. Part I: Tropical and mid-latitude water vapor fluxes. *J. Geophys. Res. Atmos.*, **125**, e2020JD032513, <https://doi.org/10.1029/2020JD032513>.
- Saliba, G., K. and Coauthors, 2021: Organic composition of three different size ranges of aerosol particles over the Southern Ocean. *Aerosol Sci. Technol.*, **55**, 268–288, <https://doi.org/10.1080/02786826.2020.1845296>.
- Salinger, M. J., and Coauthors, 2019: The unprecedented coupled ocean-atmosphere summer heatwave in the New Zealand region 2017/18: Drivers, mechanisms and impacts. *Environ. Res. Lett.*, **14**, 044023, <https://doi.org/10.1088/1748-9326/ab012a>.
- Schnaiter, M., E. Järvinen, A. Abdelmonem, and T. Leisner, 2018: PHIPS-HALO: The airborne particle habit imaging and polar scattering probe—Part II: Characterization and first results. *Atmos. Meas. Tech.*, **11**, 341–357, <https://doi.org/10.5194/amt-11-341-2018>.
- Simmonds, I., K. Keay, and J. Bye, 2012: Identification and climatology of Southern Hemisphere mobile fronts in a modern reanalysis. *J. Climate*, **25**, 1945–1962, <https://doi.org/10.1175/JCLI-D-11-00100.1>.
- Stith, J. L., and Coauthors, 2009: An overview of aircraft observations from the Pacific Dust Experiment campaign. *J. Geophys. Res.*, **114**, D05207, <https://doi.org/10.1029/2008JD010924>.
- Takahama, S., S. Gilardoni, L. M. Russell, and A. L. D. Kilcoyne, 2007: Classification of multiple types of organic carbon composition in atmospheric particles by scanning transmission X-ray microscopy analysis. *Atmos. Environ.*, **41**, 9435–9451, <https://doi.org/10.1016/j.atmosenv.2007.08.051>.
- Vivekanandan, J., D. S. Zrnić, S. M. Ellis, R. Oye, A. V. Ryzhkov, and J. Straka, 1999: Cloud microphysics retrieval using S-band dual-polarization radar measurements. *Bull. Amer. Meteor. Soc.*, **80**, 381–388, [https://doi.org/10.1175/1520-0477\(1999\)080<0381:CMRUSB>2.0.CO;2](https://doi.org/10.1175/1520-0477(1999)080<0381:CMRUSB>2.0.CO;2).
- , and Coauthors, 2015: A wing pod-based millimeter wavelength airborne cloud radar. *Geosci. Instrum. Methods Data Syst.*, **4**, 161–176, <https://doi.org/10.5194/gi-4-161-2015>.